Variability of Natural Methane Bubble Release at Southern Hydrate Ridge

Yann Marcon[1], Deborah Kelley[2], Blair Thornton[4,5], Dana Manalang[3], Gerhard Bohrmann[1]

[1]MARUM – Center for Marine Environmental Sciences and Department of Geosciences, University of Bremen, Bremen, D-28359, Germany.

[2]School of Oceanography, University of Washington, Seattle, USA.

[3]Applied Physics Lab, University of Washington, Seattle, USA.

[4]Centre for In situ and Remote Intelligent Sensing, Faculty of Engineering and Physical Sciences, University of Southampton, Hampshire, UK.

[5]Institute of Industrial Science, The University of Tokyo, Tokyo, Japan.

Corresponding author: Yann Marcon (ymarcon@marum.de)

Key Points:

- Fluctuations of methane emissions from the Southern Hydrate Ridge summit are modulated by the barotropic tide
- Permeability changes in shallow hydrate-bearing sediments cause local pressure buildups that produce strong short-term venting variability
- Distinct vents have different ebullition behaviors and monitoring a single vent would give an incomplete picture of the venting dynamics

Abstract

Current estimations of seabed methane release into the ocean (0.4 to 48 Tg yr^{-1}) are based on short-term observations and implicitly assume that fluxes are constant over time. However, the intensity of gas seepage varies significantly throughout a seep lifetime. We used instruments operated by the Ocean Observatories Initiative's Regional Cabled Array to monitor variations of gas emissions over the entire Southern Hydrate Ridge summit. We show that bubble plumes emanate from distinct and persistent vents. Multiple plumes can occur within each vent and the location of their outlets may shift progressively. Active bubble plumes vary temporally in number and intensity, even within single vents. Gas emission fluctuations are partly periodic and linked to the local tide. However, short-term variability and high ebullition events unrelated to tidal cycles are also commonly observed. Our data indicate that small-scale processes beneath or at the sediment surface are responsible for the short-term variability of the venting activity that is otherwise modulated by tides. Furthermore, a decrease of venting at one vent may coincide with an increase in plume activity at other vents. Our results depict a spatially and temporally dynamic seep environment, the variability of which cannot be fully characterized without systematic and comprehensive monitoring of the entire area. These results indicate that flux estimations may be largely overestimated or underestimated depending on the time, duration, and place of observation. Although sudden ebullition bursts are hardly predictable, we argue that tidal cycles must be taken into consideration when estimating gas fluxes.

Plain Language Summary

Methane emission from the seabed into the ocean occurs naturally along continental margins. Methane release in the form of bubbles commonly escapes the seabed and rise through the water column forming bubble plumes. Since methane is a potent greenhouse gas, understanding which factors influence the methane release rate from submarine sources is important. This study focuses on one submarine source, Southern Hydrate Ridge, located in the Northeast Pacific 85 km offshore Oregon at a 780 m water depth. We used instruments installed at the seafloor and operated through an underwater cabled observatory to monitor bubble plumes and to study why their intensity varies over time. We confirmed that pressure variations caused by tides affect methane release rate and that bubble plumes are more intense during decreasing tides than rising tides. However, we found that not all fluctuations could be accounted for by tides and that distinct bubble plumes could have decoupled behavior. The data suggest local and temporary permeability changes near the sediment-water interface as the most likely cause of the short-term gas emission variability. These findings are significant because they show that methane flux estimations from submarine sources may be largely inaccurate if based on short-term or small-scale measurements.

1 Introduction

Natural release of methane gas from the seabed occurs at cold seeps along most continental margins (Kvenvolden and Lorenson, 2001). The released methane gas can be either dissolved in seawater or gaseous in the form of bubbles. Unlike dissolved gases, gas bubbles can rise several hundreds of meters through the water column in a relatively short time, as was observed at natural seeps in the Guaymas Basin (Merewether et al., 1985), on the Carolina continental rise (Paull et al., 1995), along the Cascadia Margin (Suess et al., 2001; Heeschen et al., 2003; Philip et al., 2016a), in the Okinawa Trough (Shitashima et al., 2008), in the Black Sea (Greinert et al., 2006; Körber et al., 2014), in the northern and southern Gulf of Mexico (MacDonald et al., 2002; Römer et al., 2019), and at experimental gas plumes in Monterey Bay (Rehder et al., 2002). Gas bubbles in shallow (< 100 m) water areas may sometimes reach the ocean surface and release the gas into the atmosphere (McGinnis et al., 2006; Myhre et al., 2016; Silyakova et al., 2020). In deep water areas, the bubble methane content is believed to be rapidly lost within the water column through dissolution, oxidation and bacterial degradation (Leifer and Patro, 2002; Holzner et al., 2008; Philip et al., 2016a; Leonte et al., 2017). At depths where gas hydrates are stable, however, a hydrate coating may slow down the bubble dissolution, allowing the bubble to reach shallower depths (Rehder et al., 2009). Overall, the contribution of deep-sea methane to the global carbon budget, and especially to the atmospheric carbon is believed to be small in comparison to other carbon sources (Kvenvolden and Rogers, 2005; IPCC, 2013; Weber et al., 2019; Saunois et al., 2020).

To date, the spatial variability and temporal fluctuations of methane gas fluxes from seabed sources are scarcely investigated, leaving global estimates poorly constrained (Ferré et al., 2020). Although the causes of temporal variations likely vary from seep to seep due to site-specific differences (e.g. source of methane, subsurface structure), some common external parameters are known to influence bubble fluxes across sites. Hydrostatic pressure variations, caused by the action of tides, swell, or storms can modulate gas ebullition in both shallow (Boles et al., 2001; Leifer and Boles, 2005; Schneider von Deimling et al., 2010; Mau et al., 2017) and deep seep areas (Torres et al., 2002; Römer et al., 2016; Sultan et al., 2020). Sultan et al. (2020), further suggested that sea level rise and resultant rise in hydrostatic pressure, could durably reduce the rates of methane release from the seafloor. Additionally, increased hydrate dissociation linked to seasonal temperature variations (Berndt et al., 2014), ocean warming (Hautala et al., 2014) and even to isostatic rebound (Wallmann et al., 2018) have been linked to amplified methane gas release. Finally, increased gas released has also been observed in various sites following seismic tremors (Field and Jennings, 1987; Hasiotis et al., 1996; Obzhirov et al., 2004; Kuşçu et al., 2005; Mau et al., 2007; Fischer et al., 2013).

Hydrate Ridge is an anticlinal ridge on the accretionary wedge of the Cascadia subduction zone (Tryon et al., 1999) that hosts two well-studied methane seep areas along its north-south trending summit - Northern and Southern Hydrate Ridge (NHR and SHR). It is characterized by massive methane hydrate deposits in the shallow subsurface, authigenic carbonates, chemosynthetic fauna, and persistent gas emissions that form bubble plumes (e.g. Bohrmann et al., 1998; Suess et al., 2001; Heeschen et al., 2003; Boetius and Suess, 2004; Philip et al., 2016a). Seismic profiles of SHR show that the bottom simulated reflector (BSR), marking the base of the gas hydrate occurrence zone, is located about 125 m below seafloor (mbsf). The base is directly above the seismic horizon A, a stratigraphic layer along which methane-rich fluids migrate toward the summit of SHR from the accretionary complex (Tréhu et al., 2004a, 2004b). Hydrate Ridge bubble plumes are known to be highly variable, however, unlike the northern summit, the fluctuations of gas emissions emanating from SHR have not been linked directly to tidal cycles (Tryon et al., 1999; Torres et al., 2002; Heeschen et al., 2003; Kannberg et al., 2013; Philip et al., 2016a). Venting at SHR is thought to alternate between active and inactive phases caused by cycles of gas hydrate seals and buildup of pore pressure below the BSR, each lasting several years (Bangs et al., 2011; Daigle et al., 2011). Recent work using repeated ship-based hydroacoustic surveys, detected multiple simultaneous acoustic flares (indicative of bubble plumes) over the SHR summit, a ~60 m tall carbonate structure (the Pinnacle) located west of the summit, and within the moat area between the summit and the Pinnacle (Philip et al., 2016a). The bubble plumes were not all active during all surveys, but did re-occur in the same locations. Active venting showed variability over hourly timescales. Philip et al., (2016a) highlighted the need for systematic long-term monitoring to understand the processes controlling the variability of submarine gas emissions.

Systematic acoustic monitoring of gas emissions has been done at several marine seeps, albeit mostly for short durations from a few hours to a few days (Greinert, 2008; Schneider von Deimling et al., 2010; Bohrmann et al., 2011; Bayrakci et al., 2014; Sahling et al., 2017). Römer et al. (2016) is the only work, which used a rotary multibeam sonar connected to a cabled observatory to monitor gas emissions for over a year and with a time-resolution sufficient to analyze hourly variations. The results revealed a tidal influence on the strength of gas emissions in the Clayoquot Slope. However, the sonar range was unable to capture all gas emissions within the seepage area, making the data quality dependent on the direction of bottom currents.

In this study, we used the Southern Hydrate Ridge Overview Sonar (SHROS), a multibeam sonar connected to the Ocean Observatories Initiative's (OOI) Regional Cabled Array (RCA) (Marcon et al., 2019) to monitor all gas emissions over the entire SHR summit (Figure 1). Here we present the results from the systematic monitoring of all vents at the summit and analyze the temporal variability of their gas emissions and spatial variability. To support interpretation of the sonar data, measurements from other cabled infrastructure including two cameras, a single beam sonar, a CTD instrument, and three ocean bottom seismometers (OBS) were utilized (Figure 1). Our results confirm that localized and shallow seafloor dynamics are likely the main factors that imprint a stochastic component to the variability of the gas emissions that are otherwise modulated by the tide.

2 Methods

2.1 Acoustic monitoring of gas emission

Monitoring of gas emissions was done with the Southern Hydrate Ridge Rotating Sonar (SHROS) (Marcon et al., 2019). The SHROS consists of a multibeam echosounder (R2Sonic 2022) mounted on a rotator, with a rotating range of 360°. The echosounder swath has an opening angle of 88° and is orientated vertically, in a fashion similar to that presented by (Römer et al., 2016). The SHROS monitors the magnitude of the acoustic backscattering caused by insonified gas bubble plumes in the water column. The presence of gas bubbles in the water column generates strong, conspicuous backscatter anomalies, which can easily be discriminated from other reflectors using a combination of point clustering and filtering methods (Marcon et al., 2019). More detailed information about the SHROS design and data processing is available in Marcon et al. (2019).

The echosounder operated at a sounding frequency of 350 kHz and a range setting of 200 m, allowing it to monitor the entire summit of SHR (Figure 1). At this frequency, the beamwidth at nadir is approximately 1.3°. The time-variable gain (TVG) was computed using the two-way spherical spreading loss coefficient ($20 \log r$, where r is the range in meters) appropriate for multiple distributed targets (Moszyński and Stepnowski, 2002; Stepnowski and Mitchell, 1990). The absorption coefficient was calculated with the formula from Ainslie and McColm (1998) for the selected frequency and the in-situ conditions of temperature, salinity, and pressure. The assumption that bubble plumes constitute distributed targets is a reasonable choice at close range, but it might not accurately represent bubble plumes located farther away because the size ratio between bubble plumes and acoustic bin in the far field is far smaller than in the near field and approaches that of a single target. Should this caveat be true, the acoustic magnitude of a plume located far from the sonar is expected to be lower than the magnitude of a plume of equal size located closer to the sonar.

The SHROS collected data from 6 July 2018 to 11 November 2018 (Figures 2 and S1). Unfortunately, several gaps interrupt the data timeseries due to downtimes of either the instrument or the cabled array (Table S1). The sonar scanning sector was reduced from 360° down to 245° after 10 October 2018 because of technical problems. As a result, plumes from Einstein's Grotto and Summit-A (Figure 1) could not be monitored fully depending on the direction of bottom currents. To prevent bias in our results, we excluded all plumes recorded at these two vents after October 10 from our analyses. Furthermore, the sonar settings were modified several times over the course of the monitoring period to improve the quality of gas bubble detection, which hinders comparing magnitude data collected with different settings. The relationship between backscattering magnitude and bubble flux is nonlinear and flux quantification is currently not possible with this instrument. In this study, we consider the backscattering magnitude as a qualitative indicator of the intensity of gas emissions: high (or low) magnitudes indicate strong (or weak) gas release rates. This is reasonable because the operating frequency is outside of the theoretical resonance frequency range for the bubble radii expected at SHR (Heeschen et al., 2003; Rehder et al., 2002). The resonance bubble radius for a frequency of 350 kHz and a water depth of 750 m is about 0.08 mm, i.e. well below the usual range of bubbles issuing from seeps (0.25-0.5 to 10 mm) and we do not expect resonance effects to cause extra noise in the SHROS data. Groundtruthing using camera observations confirmed that such qualitative interpretation of the SHROS acoustic data is reasonable (see Results). A video file showing all SHROS scans is provided as an electronic supplement (Movie S1).

We also used a single-beam scanning-sonar (multi-frequency Kongsberg 1171-Series) connected to the OOI Regional Cabled Array (RCA) (instrument QNTSRA101) to provide finer spatial and temporal resolution of the bubble release at the Einstein's Grotto vent. For this work, the sonar operated at a frequency of 1200 kHz, corresponding to a beamwidth of 28° x 0.6°, and with a range set to 10 m. The resonance bubble radius at this frequency and water depth is about 0.02 mm. The sonar conducted 360° scans continuously for a duration of one day (14-15 November 2019). The rotation speed was set to the slowest setting, which corresponds to a full scan every 213 to 214 seconds. The resulting 405 scan images were compiled in a video file (Movie S2).

2.2 Optical monitoring of bubble plumes

Two photo cameras connected to the RCA were used to provide visual groundtruthing information about the dynamics and strength of bubble release. For each camera, the still images were timestamped and compiled into video files to delineate temporal changes. These are provided as electronic supplements (Movies S3 and S4).

The CAMDSB103 camera (Kongsberg 0484-6002 Color Digital Still Camera with 5MP resolution) was deployed at the Einstein's Grotto site, one of the most active seep areas of the SHR (Figure 1). The camera recorded an image sequence every 30 minutes from 1 July 2018 to 23 June 2019, covering the entire duration of the acoustic monitoring (Figure S1). Each image sequence consists of a series of three RGB images taken at a 3 Hz rate.

The CAMPIA101 camera (Sub-C Imaging Rayfin camera with 4K resolution) was deployed at the Summit-A vent area (Figure 1). The camera recorded three pictures every 30 minutes and one 30-second 4K video sequence every 2 hours from 24 July 2019 until 22 January 2020. The camera footage was used to analyze the seafloor and bubble release dynamics and to estimate bubble rise velocities. An 80 cm-long vertical measuring scale was placed next to an active bubble stream within the camera field of view to measure the distance travelled by the bubbles to estimate bubble rise velocities. The rise velocities were estimated from the 30-second 4K video sequences for the bubble stream that is located directly adjacent to the measuring stick. Other bubble streams occur within the field of view, but their rise speeds cannot be estimated due to the absence of a scale. The 4K video sequences can be downloaded from the University of Washington server for the PI-added instruments (direct link: http://piweb.ooirsn.uw.edu/marum/data/CAMPIA101/Videos/).

We used the CAMDSB103 camera to also estimate the strength of bubble release by counting the average number of bubbles visible in each image sequence. Because of the large number of images (144 images per day), the bubble counting was automated using the method illustrated in Figure S2. First, all images were cropped to retain the area of bubble occurrence and to remove all non-necessary parts of the images. This made the algorithm faster and less prone to false detections. Next, a Gaussian blur filter (sigma = 2) was applied to the cropped images to reduce high-frequency noise. Within each sequence of 3 images, the constant background was removed by negating consecutive images per in the workflow described by Johansen et al. (2017). The resulting images show the differences between the original images, i.e. moving objects such as bubbles, marine snow, and the occasional fish or crab. Only the green channel of the difference images was retained, which was the least noisy and the best suited channel for bubble detection. Using intensity thresholding, the resulting images were converted to logical black and white images, on which all moving objects appeared as white patches. All connected components of white pixels were aggregated. Objects smaller than a set pixel size (defined based on estimation of minimum size of bubble objects from visual image inspections) were filtered out. To reliably differentiate bubbles from marine snow, we relied on the fact that the bubble rising speed is too fast to be resolved by the camera. Hence, bubbles consistently appear as conspicuously elongated objects, whereas marine snow is generally rounder. Using a roundness index, a dimensionless value ranging from 0 (not round) to 1 (perfect circle) and defined by

$$Roundness = 4\pi \frac{A}{P^2}$$

with A the surface area and P the perimeter of the 2D objects on the photo, all objects were filtered out with a roundness above an empirically chosen threshold (0.5). The remaining objects are considered to be bubbles. The average number of bubble per image in each sequence were used. Visual inspection of photos with low, medium and high bubble counts showed this bubble detection method to be dependable, with an error of about 5 bubbles per image. Images with bubble counts below five were commonly caused by false positive detections. All steps of the bubble counting were done by a MATLAB script (Dataset S1).

2.3 Microbathymetry and photomosaics

The microbathymetry was acquired with the autonomous underwater vehicle (AUV) Sentry in 2008 during a University of Washington survey cruise aboard the R/V *Thomas G. Thompson* (TN221) in support of the OOI RCA installation at this site in 2014 (Figure 1). Bathymetric data were collected using a Reson 7125 multibeam sonar with a nominal survey height of 75 meters. A long-baseline transponder system was utilized to place survey lines (most spaced at 225 meters) into geodetic coordinates.

Data for the 3D photomosaic were collected by the AUV AE2000f of the University of Tokyo, equipped with the SeaXerocks 3 3D mapping system during the Schmidt Ocean Institute FK180731 #Adaptive Robotics expedition (Yamada et al., 2021). The map generation was based on known reconstruction methods (Johnson-Roberson et al., 2009; Thornton et al., 2016). The 3D mosaic has a square area of 118,000 m^2 at sub-centimeter resolution, covering the SHR summit and the SHROS monitoring area almost entirely (Figure 3).

2.4 Physicochemical data

In-situ environmental parameters were recorded with a CTD probe (Sea-Bird Electronics SBE16plusV2 SeaCAT) equipped with a dissolved oxygen optode sensor (Sea-Bird Electronics SBE63) and a flushing pump (Sea-Bird Electronics SBE5T). All sensors were calibrated by the manufacturer in April 2018 and installed at SHR in June 2018 during the VISIONS'18 expedition with R/V *Roger Revelle*. The CTD probe was mounted on a 1-m tall tripod and the conductivity, temperature, pressure, and dissolved oxygen concentration of the bottom water was measured every minute (the pump inlet was located approximately 30 cm above the seabed). All sensors were flushed for 40 seconds before every sample. Each sample is an average of 20 consecutive measurements (taken at a 4 Hz rate). The CTD probe collected nearly continuous data until recovery in August 2020 (Figure S1). The CTD data were used to compute the in-situ sound velocity (SBE Application Note No. 6, 2004) and sound absorption (Ainslie and McColm, 1998) used by the SHROS.

High-frequency tidal seafloor pressure was recorded at a 1 Hz sampling rate with a tsunami pressure sensor (Sea-Bird Electronics SBE 54). For spectral analyses, the pressure data of the tsunami pressure sensor were utilized. The SBE 54 sensor was located on the LJ01B junction box (Figure 1) about 10 m deeper than the CTD probe, but it has a depth resolution higher than 1 mm and is free of instrument drift. By contrast, the CTD pressure data were affected by strong instrument drift from December 2018 onward.

2.5 Current velocities

Current velocities were provided by an upward-looking acoustic Doppler current profiler (Teledyne RDI Workhorse Long Ranger ADCP 75 kHz) operated by the OOI RCA. The ADCP is located on the MJ01B junction box (Figure 1) and measures current velocities every 2.5 seconds for every 8 m-thick depth bins between about 760 m water depth and the sea surface. To prevent acoustic interference with the SHROS (Marcon et al., 2019), the ADCP was scheduled to stop pinging for exactly 15 minutes every two hours, when the SHROS was operating.

Northward, eastward and upward velocity constituents were plotted from 01 June 2018 until 29 February 2020 using 15-minute averages for the lowest 500 m of the water column to facilitate the visualization of bottom currents. The plots are provided as an electronic supplement (Dataset S2).

2.6 Seismic data

Seismic data were recorded by an array of three ocean bottom seismometers (OBS) operated by the OOI RCA and connected to the LJ01B junction box (Figure 1). All OBS data were downloaded from the IRIS Data Management Center (www.iris.edu). We used timeseries data from two short-period OBS (Guralp CMG-6TF) and one broadband OBS (Guralp 1T/5T/DM24). The buried broadband OBS is located close to the LJ01B junction box, about 120 m southwest of the center of the SHR summit area (Figure 1) and is suitable to detect regional seismicity and earthquake activity. The short-period seismometers are located about 450 m to the northeast and 360 m to the southeast of the summit. They can detect smaller vibrations caused by local phenomena.

For all OBS measurements, we used the 1 Hz timeseries for East, North and vertical directions (LHE, LHN, LHZ seismic channels) to visualize times when amplitudes of bottom movements exceeded the background noise, as well as to determine the dominant frequency constituents of the signals. The 8 Hz timeseries (MH seismic channels) were used to detect short-duration seismic events (SDE) by applying a applying a short-time average/long-time average algorithm (STA/LTA) as described by Tsang-Hin-Sun et al. (2019). The parameters used were 0.3 second and 7 seconds for the STA and LTA window, with a trigger threshold of 5, in order to restrict the detection to the high-amplitude SDEs of the seismic record. Additionally, for the highest amplitude non-SDE tremor detected with the short-period seismometers during the SHROS monitoring, the 200 Hz timeseries (EH seismic channels) were used to identify the timing of the first-arrival of P-waves and S-waves with greater accuracy, to estimate the distance of the source of the seismic vibrations.

2.7 Wave height

To test whether wave-induced pressure variations influence the seabed gas release wave height data were downloaded from the National Data Buoy Center of the National Oceanographic and Atmospheric Administration (NOAA) for the surface buoy that is closest to the SHR. The OOI-operated Buoy #46098 "OOI Waldport Offshore" is located 25 km southeast of SHR. The water depth at this location is about 575 m according to the GEBCO gridded bathymetry data (www.gebco.net). The significant wave height was used, which corresponds to the average of the highest one-third of the wave heights measured in a 20-minute window.

2.8 Spectral analyses

Discrete Fourier spectra were computed to identify the main constituent frequencies in each timeseries of data. The DC component was removed and Hamming windows (of the same length as the timeseries) were applied to each timeseries. Because of large gaps in the acoustic data, the Fourier analyses were only computed for selected segments of the timeseries. For all other datasets, the discrete Fourier transforms (DFT) were applied to the longest gapless segments that encompass the selected acoustic data segments.

In terms of quality and length, the acoustic data segments 06.07.2018-22.07.2018 and 19.10.2018-08.11.2018 are the best suited to conduct frequency analysis (Table S1). The second segment comprises one 8-hour gap, which was zero padded for the purpose of the spectral analysis. Based on the duration of the segments (16 and 20 days) and the sampling frequency (Ts = 2 h), they are suited to analyze constituent frequencies with periods no shorter than 4 h (Nyquist frequency) and no longer to 8 and 10 days. Periodic variations of the gas release with frequencies outside of this range (0.1 to 6 cycles per day, or cpd) cannot be investigated with the current timeseries.

3 Results

Pressure data from the CTD and the tidal seafloor pressure probe show clear tidal variations with amplitudes ranging from about 1.4 dbar during neap tides and up to 3.8 dbar during spring tides. Spectral analysis of the pressure data (1 June 2018 to 23 March 2020) reveals five strong frequency peaks, centered on periods of 12.42 h, 23.93 h, 25.82 h, 12 h and 12.66 h (from strongest to the weakest). These frequencies correspond to the semi-diurnal (M2, S2, N2) and diurnal (K1, O1) constituents of the mixed tide regime along the Oregon coast (Harmonic Constituents for 9435380, South Beach OR, NOAA Tides & Currents, https://tidesandcurrents.noaa.gov/harcon.html?id=9435380) and they explain about 98% of the variance for frequencies between 1/7 cpd (weekly) and 24 cpd (hourly). The power of semidiurnal constituents is about 3.4 times higher than the power of the diurnal constituents.

The bottom water temperature at the SHR summit ranged from 3.8 °C to 4.5 °C (mean: 4.178 °C, std.: 0.106 °C) between June 2018 and November 2018 (monitoring period of the SHROS, Figure S3), and from 3.7 °C to 4.7 °C (mean: 4.146 °C, std.: 0.116 °C) between June 2018 and June 2020 (Figure S4). The latter temperature timeseries, which spans 2 years, did not show evidence for a long-term warming or cooling of the bottom water at the SHR. Practical salinity values between June 2018 and November 2018 (Figure S3) ranged from 34.26 to 34.37 psu (mean: 34.31, std.: 0.02) with variations opposite of the temperature variations. The dissolved oxygen levels varied between 0.24 and 0.30 ml/L (mean: 0.27 ml/L, std.: 0.01 ml/L), corresponding approximately to 10.4 to 13 µmole/kg (mean: 11.74 µmole/kg, std.: 0.43 µmole/kg) highlighting strong anoxic conditions at the SHR. Absolute salinity and oxygen values after November 2018 are not reported because of increasing measurement drift. The variations of temperature, salinity, and oxygen concentrations in background bottom water near the SHR summit (Figure S3) correlate poorly with the bottom pressure data (temperature: $r = 0.26$, salinity: $r = -0.30$, oxygen: $r = 0.06$) but show semi-diurnal variations, reflecting a tidal influence on these parameters. Relatively large variations occur over multiday timescales, which do not appear linked to the tidal pressure and may relate to seasonal variations of the bottom current regimes. Spectral analyses of the temperature and practical salinity data show large peaks at the frequencies corresponding to the semi-diurnal (M2, S2, N2) tidal constituents, and relatively weak diurnal (K1, O1) constituents.

The SHROS conducted scans every 2 hours from 6 July to 8 November 2018, with a few gaps in the timeseries data due to downtimes of the system (Table S1). In total, the sonar recorded 888 scans during the monitoring period. Gas flares were detected in 99.8% of the scans (886 out of 888 scans), suggesting that the gas bubble release was continuous. The summed magnitude of all detected plumes show large intraday variations, with alternating peaks and troughs, which we interpret as variations in intensity of the gas emissions. Both magnitude peaks and troughs occurred about twice a day, reflecting a semi-diurnal periodicity. The magnitude data also tended to show higher peaks during spring tides than during neap tides. However, due to gaps between data segments, longer multiday trends cannot be unambiguously identified.

The distribution of bottom pressure during magnitude peaks (> 75% percentile of magnitude data) between 6 July and 22 July and between 19 October and 8 November (i.e. the longest uninterrupted timeseries of SHROS data) indicate that intense gas emissions can occur at any pressure within the tidal pressure range (CTD data: 778.7 to 782.4 dbar, mean: 780.7, std.: 0.75), however, they are twice as frequent at low and decreasing bottom pressures. For each time segment, at least two thirds of all the peaks (65-70%) coincide with pressures lower than the average pressure. Of the remaining 30-35% of the peaks, which occurred at pressures exceeding the mean value, 65-70% occurred during decreasing tide, 18-20% occurred at the high tide turning point, while less than 15% occurred during rising tide. These observations suggest that gas emissions are more intense at low tides than at high tides (Figure 2), and that decreasing and low tidal pressures facilitate the escape of gas from the seabed. However, large peaks were also recorded during rising and high tide. The strongest anomaly in the July timeseries occurred at pressures above the mean value and during rising tide, an indication that large bubble release events may also occur independent of the tide.

Spectral analyses of the two longest timeseries of SHROS data, from 6 July to 22 July (about 16 days) and from 19 October to 8 November (about 20 days), identified dominant constituent frequencies with periods between 11.80 h and 13 h. These frequencies coincide with the semi-diurnal (M2, S2, N2) tidal constituents and they account for about 25% of the variance of both timeseries for frequencies between 1/7 cpd (T = 7 days) and 6 cpd (T = 4 h) (Figure 4). Smaller frequency constituents with periods between 24-25 h corresponding to the diurnal (K1, O1) tidal constituents may also be present, but their power is too weak to be identified clearly from the noisy frequency spectrum.

The SHROS acoustic flare images show that the number of active bubble plumes varied highly throughout the monitoring period and were comprised of between 1 and 8, with an average of almost 4 plumes (standard deviation: 1.1). Five main clusters of activity were observed based on the spatial distribution of the flare base points (Figure 3): Smokey Tavern, Einstein's Grotto, Summit-A, Summit-B, Summit-C. These main plume clusters represent the main vent sites at the SHR summit and with diameters of 10 m to 30 m. Bubble release at these main vent sites is frequent, but intermittent and it can pause for several days in a row, although hardly ever simultaneously at all sites (Figures 5 and S5). Multiple bubble streams can escape simultaneously from the same site (up to 4 at Summit-C and up to 3 at Einstein's Grotto, Smokey Tavern, Summit-A and Summit-B). According to flare images and camera observations, simultaneous bubble plumes within the same vent may be of very different intensities. This indicates that very shallow seafloor permeability changes influence bubble release (see Discussion). In addition to the main vent clusters, at least six smaller clusters of activity were detected: Smokey Tavern West, Summit-D, Far NE, Far S, Summit South, and Summit SW. These smaller venting sites are located farther away from the center of the SHR summit. Bubble release at these periphery sites is comparatively seldom and can pause for weeks or months, but at times generate large acoustic flares.

The microbathymetry and photomosaic (Figure 3) show that the main vents are located in areas where the seafloor is uneven and covered by white microbial mats. These areas are characterized by slightly up-domed mounds that extend laterally over dozens of meters each, up to about 35 m at Smokey Tavern. Parts of the domed mounds form hummocky, jagged depressions that appear to be eating away at the dome structures (Figure 3d), likely caused by vigorous seepage (See results from CAMPIA101). The acoustic flare clusters appear to be focused on the hummocky areas at the main vent sites, with the exception of Smokey Tavern, confirming that these hummocky areas are linked to venting. At Smokey Tavern, the flare points spread over the entire up-domed and microbial mat-covered area. The limit between Summit-B and Summit-C is ambiguous as the two distinct plume clusters originate from a hummocky area that stretches over two sides of the same dome. The periphery vent sites are located close to small mounds covered with carbonate hard grounds. Plumes at the periphery vents do not seem to originate from the mounds, but from locations near the mounds where dark sediments and white microbial mats can be seen on the photomosaic.

Figure 5 depicts the SHROS magnitude data from 6 July to 22 July 2018 for each of the six main clusters. Figure S5 shows the SHROS data from 19 October to 8 November 2018, for the active vents that were located within the restricted 245° scanning sector. The vertical axis scaling is logarithmic to discern low magnitude variations as well. The mean magnitude of the main clusters is highest for the clusters closest to the SHROS, such as Summit-A and Summit-B and lowest for the ones farthest from the sonar, such as Summit-D and Smokey Tavern. The sites nearest to the sonar are also closest to the center of the SHR summit. It could be that the central sites are more active than decentered sites or that the parameters of the time-variable gain (TVG) curve we used during the SHROS surveys (Table S1) did not fully compensate the sound transmission losses, which depend on the distance between the sonar and the targets. The latter explanation is more probable given that we used the 'default' two-way spreading loss coefficient for the sonar (see Methods) that is normally used for distributed targets such as the seabed or fish schools. In this case, the mean acoustic intensity of clusters located at different distances from the sonar cannot be compared. However, comparing the temporal variations is possible.

The data confirm the observations from acoustic flare images that no cluster was continuously active during the monitoring period, although venting from the SHR summit never fully ceased. Between 6 July and 22 July 2018 the flare clusters can be ranked from most frequently active to least frequently active as follows: Summit-A (active 75% of the time), Einstein's Grotto (69%), Smokey Tavern (65%), Summit-B and Summit-C (54%), Summit-D (22%), Far NE (9%), Far S (2%), Smokey Tavern West (1%). During this period, Summit South and Summit SW were completely inactive. The activity of the flare clusters between 19 October and 8 November 2018 was as follows: Smokey Tavern (44%), Summit-B (30%), Summit-C (70%), Summit-D (23%), Smokey Tavern West (6%). Commonly, a magnitude decrease at one or more clusters coincided with an increase at other clusters, which suggests that the fluctuations of the venting activity of the different sites are interdependent. For example, an increase in venting at Summit-C was coincident with a pause in venting at Summit-A around 10-12 July. Summit-A and Summit-B became active again on 12 July, just before Summit-C stopped venting. Between 19 October and 8 November, Summit-B was active mostly when Summit-C was inactive (Figure S5). Several such apparent connections are supported by the data, which indicate that these relationships may not be purely coincidental. In the frequency domain, the magnitude data for the main clusters show peaks corresponding to the semi-diurnal tidal constituents, indicating that the tides also influence the venting activity of individual clusters (Figures S6 and S7).

The high-temporal resolution survey with the scanning-sonar located in the Einstein's Grotto area showed variations of three bubble plumes for a duration of 24 h, with a time resolution of about 3.55 minutes (213 to 214 sec/scan). Bubble release was continuously active during the monitoring period, but the plume intensities varied significantly over time and were punctuated by several high ebullition events that occurred either at decreasing tide or right at the turning point between flood and ebb tides. High ebullition events were characterized by large acoustic flares with much stronger intensity than the usual 'background' flares (Figure 6). Each high ebullition event had a sudden onset and a slower decline. Some high ebullition events affected the three bubble plumes sequentially each within less than 3.55 minutes (i.e. one sonar scan) of the previous one.

Photo data from the CAMDSB103 camera from 1 July to 31 December 2018 provide groundtruthing information about the activity of the bubble release at the Einstein's Grotto vent site. The camera pointed towards an intense and recurrent known bubble plume at Einstein's Grotto. From July to 18 August, the timeseries of bubble counts showed large peaks, exhibiting when the bubble plume was active. No bubble release was observed on the camera footage after 18 August until the end of SHROS monitoring period (Figure S8). However, the SHROS continued to detect acoustic flares in this area after 18 August, indicating that the bubble release did not cease, but that the outlet moved away from the camera field of view. The timeseries shows a good match with the SHROS data for that particular plume (Figure 7), indicating that the sonar is effective at detecting large ebullition events and that peaks in magnitude represent events of heightened bubble release. The height of the magnitude peaks is not linearly related to the strength of the ebullition event and a few peaks have a magnitude that seems to over-represent the bubble count. This is partly due to the fact that the sonar captures the plumes up to a height of about 200 m, whereas the camera shows the bottom few meters (< 5 m). Despite this, the acoustic data and the image-derived bubble count show a weak positive correlation (correlation coefficient $r = 0.53$). This weak correlation is statistically significant (p-value for correlation: $4x10^{-15}$, $n = 191$) and indicates that the sonar data reflect the intensity of the gas emissions and that it can be used to distinguish periods of intense ebullition from less intense ones, as well as their frequency of occurrence. The sonar data cannot, however, be used for quantification purposes without a prior calibration and a detailed knowledge of the sizes and rise speeds of the bubbles within the plumes.

The CAMPIA101 camera was located at the Summit-A vent site and pointed towards a depression that cut through a domed smooth seafloor, in which bubble release was recurring. The series of footage over a period of 7 months (16 July 2019 to 22 January 2020) shows that the depression progressively widened as the walls were being eroded by bubble release, bottom currents, and possibly the loss of underlying hydrate deposits. The widening process was partly progressive, but punctuated by a few rapid events, such as the sudden release of large amounts of gas and sediments into the water column, the collapse of overhanging wall sections, and the slumping of unconsolidated sediments from the walls inside the bottom of the depression (Movie S4). In particular, the loss of loose sediments and hydrate deposits from the base of the depression walls appeared to cause the overlying consolidated sediments to overhang and ultimately to collapse. These events sometimes exposed massive gas hydrate deposits (e.g. Movie S4 on 15 October 2019 at 20:30 UTC) that were trapped under thick consolidated sediments (about 50-100 cm) and then disappeared progressively, likely through dissolution or through rafting up as the overlying sediments retreated. Bottom currents also contribute to the erosion process as shown by the gradual disaggregation of the collapsed sediment blocks. Bubble escape was intermittent but frequent throughout the monitoring period (see 4K video sequences) and at least 4 release outlets located less than 2 m apart were identified within the field of view of the camera (Dataset S3). Further outlets outside of the field of view existed near the feet of the camera tripod, as evidenced by the presence of bubble streams passing in front of the lens. Over time, the locations of some bubble outlets gradually shifted, partly due to the changes in topography. Some outlets may have become active following the accumulation of collapsed sediments around the measuring stick and the subsequent temporary closure of the bubble outlet in this area. The vigor of the bubble release of each outlet was variable over time. Several bubble release regimes were observed at each outlet: inactive, distinct single bubbles released every few seconds, clouds of bubbles of mixed sizes released in bursts, or continuous streams of bubbles. The number of active outlets within the field of view rarely exceeded one at a time, but could reach up to four simultaneous bubble streams at times, each with different release regimes. The fact that the bubble release appeared unrelated between each outlet of Summit-A indicates that the rate of bubble release of an outlet may be controlled by very shallow temporary blockages.

Bubble rise velocities were only measured at the bubble stream that was located immediately adjacent to the measuring scale (Dataset S3). Rise velocities are non-normally distributed and range from 18 to 34 cm/s, with an average of about 25 cm/s (n = 93, median = 24.1 cm/s, standard deviation = 4.3 cm/s, skewness: 1.19). Unfortunately, we could not correlate these camera observations with the acoustic data as technical failures prevented the SHROS and the CAMPIA101 to monitor the Summit-A vent simultaneously.

Similar dynamic processes were documented at the Einstein's Grotto vent. The CAMDSB103 camera showed evidence of several sudden events, caused by the apparent rapid release of gas overpressure in the subsurface during which sediments were ejected in the water column, causing seafloor changes. The largest such event occurred on 23 July 2018 between 00:46 am and 01:16 am UTC, during a rising tide about halfway between low and high tide (Figures 8 and S3). The camera shows that bubble release was active, but weak before and after the blowout. The images do not indicate an increase or decrease of bubble release within the 30 minutes after the blowout compared to the 30 minutes prior. Unfortunately, the monitoring sonars were off at this time due to technical issues and we cannot confirm whether a large bubble release accompanied the blowout. However, scans from the scanning-sonar taken before and after the blowout show that it affected the morphology of the seabed over an area of at least 3 m^2 (Figure 8).

The ADCP data show that current velocities in the top 300 m to 500 m of the water column are turbulent and relatively high (e.g. mean velocity > 50 cm/s, standard deviation > 100 cm/s in February 2019) compared to the deeper part of the water column. Depending on the season, diurnal vertical oscillations of the measured velocities occur down to a depth of 300 to

400 m, which may be linked to the diel vertical migration of zooplankton. Current velocities below this turbulent upper section have lower amplitudes (mean velocity < 15 cm/s, standard deviation < 10 cm/s in February 2019) and are vertically homogeneous all the way to the bottom. Horizontal velocities in deeper waters (below 400-500 m below water surface) display a clear semi-diurnal periodicity throughout the year as well as some seasonal variations. Near the bottom, the north-westerly currents dominate the current regime. Vertical velocities below depths of 450-500 m are almost never negative and alternate at a semi-diurnal frequency between intervals of low to null velocities (approx. 0 to +0.5 cm/s) and intervals of upwelling flow characterized by elevated upward velocities up to 20 cm/sec (Figure 9). Vertical velocities in these upwelling flows are highest close to the bottom and decrease with decreasing depth to become null around 500 m water depth. Most upwelling flows, with velocities exceeding 5 cm/s, rise about 300 m into the water column, corresponding to a depth around 470 m. Some upwelling flows could still be traced above this depth and up to depths of 400-350 m from the water surface, although once they reached this depth, the velocities were well below 5 cm/s. These upwelling flows are associated with velocity data gaps caused by outlier readings of the ADCP beam data. These recurrent data gaps affect all four beams of the ADCP indicating that they are caused by the presence of bubble plumes crossing the ADCP beams rather than by the presence of fish. Overall, the ADCP plots show clearly that the upwelling flows are closely related to the rise of bubbles in the water column (Figure 9). Upwelling flows are detected intermittently, essentially when the tidally-modulated north-westerly bottom current is either weak or reversed (Figure 9). Given the location of the ADCP in relation to the dominant bubble plumes (Figures 1 and 3), it is apparent that the dominant NW current effectively deflect bubbles plumes, and associated upwelling flows, away from the ADCP beams at a mainly semi-diurnal frequency (Figure S9).

Analysis of the broadband and short-period seismometer data series revealed no apparent connection with gas emissions or camera observations (Figure S10). The timing of heightened bubble release (sonar data) and of seabed changes (camera footage) did not coincide with ground velocities larger than background noise of the data. The analysis of high-amplitude short-duration events (SDE) detected several high-amplitude SDEs during the entire monitoring period of the SHROS. Three SDEs occurred during the 6-22 July 2018 period (Figure S11) and 41 occurred between 19 October and 8 November 2018 (Figure S12), out of which 29 are false detections that are related to the long-lasting seafloor tremor on 22 October 2018. The timing of the SDEs did not coincide with any conspicuous change in venting activity at SHR. The tremor with the highest amplitude that was recorded during the SHROS monitoring period occurred on 22 October 2018 at about 6:18 am UTC. Because of uncertainty on the exact arrival times of the P-waves and S-waves, we estimate the time lag between the two body waves to be between 1.1 and 1.3 seconds for both stations (Figure S13). Considering the measured body wave velocities for the SHR summit (Kumar et al., 2006), the epicenter of this local seismic event should be located approximately between 300 and 500 m from each station, which is compatible with a location near or over the summit. However, no connection with the sonar and camera observations could be made. Apart from these high amplitude events, which contain most of the seismic signal's power, the seismic frequency spectra for all three axes (Northward, Eastward, upward) are dominated by the main tidal frequency constituents. Higher frequency constituents can be found in the domain of the ambient seismic noise (Hilmo and Wilcock, 2020).

Wave height data recorded in 2018 by the monitoring NOAA buoy that is closest to SHR show strong seasonal variations (data not shown). Waves were generally high from January to

April and October to December, with monthly means exceeding 2 m and maximum wave heights up to almost 10 m, and comparatively low from May to September, with monthly means under 2 m and maximum wave heights below 3.1 m. Wave heights during the monitoring period of the SHROS rarely exceeded 3 m. In terms of wave heights, the SHROS monitoring period from 6 July to 22 July can be divided into two phases (Figure S14): a low phase with a mean wave height of 0.85 m between 6-11 July and a higher phase with mean wave heights around 2 m between 11-22 July. The transition between the two phases saw wave height surge of 2 m within about 24 h. The wave height data show no correlation with the acoustic data ($r = -0.06$, p-value: 0.44, $n = 191$). Wave heights during the SHROS monitoring period from 19 October to 8 November exceeded 3 m and reached up to 4 m on three occasions (Figure S15). Each of these three events lasted less than 36 h. No correlation between the timing of these events and the variations of the bubble release was observed ($r = -0.05$, p-value: 0.45, $n = 233$).

4 Discussion

4.1 Gas plume distribution

Our results show that the SHR summit hosts several distinct vents. In the following discussion, we define a vent as a distinct area of the seafloor where gas ebullition recurs. A vent can include several bubble outlets, some of which may be active simultaneously. Simultaneous bubble plumes within a vent can display very different acoustic strengths and bubble release rates.

At least five recurrent "main" vents and six less active "periphery" vents (Figure 3) were detected on the SHR summit. This amount of vents exceeds the number of vents previously detected by ship-based echosounders over the SHR summit, which was three vents at locations named Einstein's Grotto, Smokey Tavern and Summit-A (Philip et al., 2016a). In this work, we identified two additional recurrent vents located between 20 m and 60 m north of Einstein's Grotto, which we referred to as Summit-B, Summit-C, as well as several minor periphery vents. Between 6 July and 22 July 2018, the main vents were active between 54 and 75 % of the time, whereas the periphery vents were active between 0 (fully inactive) and 22% of the time. The detection of these sites benefitted from the systematic sampling strategy, which allowed the detection of rarely active vents, as well as from the high resolution, which made possible to distinguish vents that are too close to be differentiated by ship-based hydroacoustic surveys. Philip et al. (2016a) detected additional vents over the SHR Pinnacle, and half-way between the Pinnacle and the summit in a location, named Central, that is peculiarly close to the Ocean Drilling Program site 1250 (ODP Leg 204) (Tréhu et al., 2003). These sites are too far from the SHR summit and were out of range of the SHROS. However, ship-based multibeam water column surveys during the yearly OOI maintenance expeditions detected plumes at Central on 25 and 28 June 2018 (VISIONS'18, R/V *Roger Revelle*) and at Central and the Pinnacle on 26 June 2019 (VISIONS'19, R/V *Atlantis*). On 19 August 2020, (VISIONS'20, R/V *Thomas G. Thompson*) a strong plume was detected above the Pinnacle with the ship's MBES during the ebb of a spring tide. This confirms that intermittent seepage at these sites is still ongoing. Plumes over the SHR summit were detected during every survey, indicating that the venting activity is more persistent at the summit.

The high resolution of the SHROS also revealed that vents are generally not characterized by a single bubble plume outlet, but can be comprised of several bubble plumes. The spatial extent of the plume clusters detected by the SHROS (Figure 3) reflects significant variability in the locations of active outlets over time. Part of the cluster spread is explained by limits of the method in detecting the origin of acoustic flares at the seabed. Acoustic data in the first 5 meters above the seafloor were cropped out to improve the flare detection, and bubble plumes in those first meters may be deflected by bottom currents. Assuming that current speeds in the lowest 5 m of the water column are similar to those measured in the lowest ADCP bin located between 13 and 21 meters above seafloor (masf), current-driven deflection of the bubbles in the first 5 masf could cause an average horizontal drift (i.e. using average current speed) of 1 m to 2 m with a standard deviation between 0.5 and 1 m from the bubble outlet location (using the fastest and slowest bubble rise velocities). The maximum horizontal deflection distance, using the maximum current velocity and the slowest bubble rise velocity, would reach up to 12 m. This simple calculation shows that the plume deflection is not the only explanation for the spread of the plume clusters. It is clear that bubble plumes within each of the main vent sites originate from multiple outlets on the seabed and that the size of the plume clusters approximately reflects the extents of the corresponding vent area.

This result is supported by the 3D mosaic and micro-bathymetry data (Figures 1 and 3), which show that the main vents consist of up-domed and partly hummocky areas, wherefrom the strongest plumes originate. The main vents are covered by white and orange microbial mats, an indication of diffuse seepage (Boetius and Suess, 2004). Up-domed areas at SHR are linked to the occurrence of massive gas hydrates in the shallow sediments (Heeschen et al., 2003; Torres et al., 1999), the accumulation of which can cause the formation of mounds (Paull et al., 2008; Römer et al., 2012; Serié et al., 2012).

The hummocky areas were largely shaped by venting activity. The link between hummocky areas and venting at SHR has been pointed out previously (Kannberg et al., 2013) and is evidenced by our time-lapse camera observations of the Summit-A and Einstein's Grotto vents (Movies S3 and S4), which show that venting activity is very dynamic and associated with both slow and rapid seafloor changes. The combination of pressure outbursts, vigorous bubble release, loss of hydrates, and bottom currents drives erosion of the surrounding domed sediments, leading to a progressive enlargement of the rugged depressions. Loosening of sediments and loss of shallow hydrates cause the enlargement of the rugged areas and may contribute to triggering further release of free gas that was previously trapped underneath the shallow hydrates. According to past yearly ROV observations at SHR, the morphology of the Einstein's Grotto and Smokey Tavern vents changed considerably from 2011 to 2014 (Philip et al., 2016a) and until 2020 (own observations). The nature of the year-to-year changes described by Philip et al. (2016a), e.g. the enlargement of a small depression into a large pit at Einstein's Grotto and the collapse of depression walls at Smokey Tavern, is consistent with our findings.

The loss of the gas hydrate deposits from the shallow sediments is most likely driven by hydrate dissolution, i.e. the release of dissolved methane caused by hydrate exposure to non-saturated water. Because SHR lies deep within the gas hydrate stability zone (the GHSZ at SHR is approximately between 500 and 900 m below sea level) and no temperature anomaly is known to occur (Tréhu, 2006), hydrate dissociation (release of methane bubbles, caused by hydrate stability conditions not being met) is unlikely to occur in the shallow sediments (Xu and Germanovich, 2006). Furthermore, hydrate dissolution can cause depressions on the seabed

(Sultan et al., 2010), which is in agreement with our seafloor observations. We posit that local bottom currents may enhance the dissolution of shallow hydrates by scouring the hydrate-bearing sediments with unsaturated water. Such influence of bottom currents on methane seepage from outcropping hydrates have been suggested at seeps in the Barkley Canyon, off Vancouver Island (Thomsen et al., 2012). Another process that could contribute to the loss of hydrates is the detachment and rafting of buoyant chunks of hydrate-bearing sediments (Pape et al., 2011; Paull et al., 2003). Although never directly witnessed at the seafloor, the release of gas hydrate pieces at SHR has been observed at the sea surface (Suess et al., 2001) and might contribute to the formation of the rugged depressions around the vent sites.

4.2 Temporal variations

Most studies of SHR considered bubble release at the scale of the entire SHR summit leading to a large-scale picture of the system in which the bubble release at the SHR summit is either active or inactive, and supplied in free gas by the Horizon A reservoir through a network of fractures. Based on this model, the SHR venting was inferred to occur periodically with quiescent and active phases alternating over decadal timescales (Daigle et al., 2011). However, this model does not explain the local high frequency variability of the gas release. Indeed, this study and that of Philip et al. (2016a) has documented that bubble release occurs simultaneously in several places over the SHR summit, and that the activation and intensity variations of each plume can occur at intraday timescales. This is particularly clear in our results from the systematic monitoring, which show that individual plumes can start and cease over timescales as short as a few hours (< 4 h). These results also show that despite local variability, the bubble release at the scale of the SHR summit is quite persistent. Venting may have never fully ceased over the entire monitoring period of the SHROS, and it is influenced by variations in bottom pressure linked to the barotropic tide. The tidal influence was even detected at the scale of individual vents. Active vents, and even single bubble plumes, displayed strong short-period temporal variations, commonly concurrently with bottom pressure variations. However, the alternation of vent active and inactive phases does not follow a clear pattern and is not solely explained with tidal variations. An interplay between the vents is considered possible based on our data (Figures 5 and S5). In this section, we further discuss that tides modulate the active release of bubbles but that they are not the only variable controlling the onset and cessation of bubble plumes or of high ebullition events.

4.2.1 Tidal modulation

The possibility of a tidal control over the gas emissions at SHR has been subject to discussion, but previously could neither be established nor rejected because of the lack of systematic observations over multiple tidal cycles (Tryon et al., 1999; Torres et al., 2002; Heeschen et al., 2005; Bangs et al., 2011; Daigle et al., 2011; Kannberg et al., 2013; Philip et al., 2016a). Tidal influence on methane seepage for Northern Hydrate Ridge (NHR) was inferred from video observations of bubble discharge rates (Torres et al., 2002) and water column methane concentration measurements (Heeschen et al., 2005). However, no tidal correlation was observed for the SHR in the data available at the time. Additionally, repeated ship-based hydroacoustic surveys could not confirm the possibility of a tidal influence on the methane seepage at SHR (Kannberg et al., 2013; Philip et al., 2016a).

Results of SHROS acoustic monitoring of bubble plume activity show clear semi-diurnal and possibly diurnal periodicities, providing strong evidence that the total methane bubble release at the SHR is tidally modulated. This is further supported by the timing of the peaks in the SHROS data, which show that peaks in bubble release are twice as likely to occur at decreasing or low tidal pressures.

The influence of the tides on gas emissions has been measured or inferred at several seep sites before. In particular, acoustic monitoring using a rotating multibeam echosounder connected to the Neptune observatory of Ocean Networks Canada, confirmed that bubble release in the 1250 m-deep Clayoquot Slope is modulated by the semi-diurnal constituent of the local mixed tide regime (Römer et al., 2016). At shallow seeps (< 70 m) near Coal Oil Point, Boles et al. (2001) measured that the seep flow rate decreased at high tide and increased at low tide, and that one meter increase of sea height led to a reduction of up to 2.2% in flow rate. Such quantification of the flow rate response to tidal sea height changes is not available for deeper seeps. Whether, and to what extent, increasing depth affects the tidal influence on bubble release from the seabed is unclear.

The current understanding is that methane bubble fluxes tend to be higher when bottom pressure decreases (Martens and Val Klump, 1980; Jackson et al., 1998; Tryon et al., 1999; Boles et al., 2001; Leifer and Boles, 2005; Schneider von Deimling et al., 2010; Römer et al., 2016). Tidal loading and unloading cycles cause sediment pore pressure and permeability variations (Wang and Davis, 1996) that affect the rate of gas release. Decreased hydrostatic pressure during low tides facilitates the opening, or dilatation, of fractures and makes it easier for pore gas pressure (P_g) to overcome the total stress (σ), leading to rapid gas discharge (Tryon et al., 1999, 2002; Leifer and Boles, 2005; Liu and Flemings, 2009; Scandella et al., 2011). Recently, in-situ pore pressure measurement in gas-rich sediments on the Vestnesa Ridge (NW Svalbard) at water depths ranging from 910 and 1330 m confirmed that tidally-driven fluctuations of hydrostatic pressure generate local pore pressure gradients, which facilitate the release of gas into the water column during decreasing tide (Sultan et al., 2020). These mechanisms are generally well-supported by our results because the frequent increase of gas emissions we observe during tidal unloading is compatible with a pressure control on active gas emissions.

According to Scandella et al. (2011), the amount of gas released into the water column depends on the depth from which the flow conduits dilate, which in turn depends on the magnitude of the hydrostatic pressure drop. Given that there is evidence for free gas not only below the BSR, but also within conduits throughout the GHSZ at SHR (Tréhu et al., 2004a, 2004b; Liu and Flemings, 2006), such a conduit dilatation model supports our observation that gas emissions appear to be more intense during spring-tides compared to neap-tides. Spring-tides are characterized by higher amplitudes of hydrostatic loading/unloading cycles and flow conduits are likely to dilate deeper than during neap-tides, potentially causing higher gas release. Although the tidal amplitude may influence the strength of gas release, the distinct vents we monitored had different behaviors in terms of bubble release, indicating that their activity is not solely linked to the pressure cycles.

It is evident that other less predictable factors contribute to the variability of individual vents. A vent that recently released many bubbles might contain a smaller amount of free gas within the sediment (Maeck et al., 2014) and temporarily respond more weakly to following pressure variations. Tidal cycles also affect the solubility of gas in pore water (Wang et al., 1998) and the exsolution of gas from the pore water at decreasing bottom pressures may contribute to increasing bubble emissions at low tide (Leifer and Boles, 2005; Römer et al., 2016). Römer et al. (2016) suggested that methane exsolution caused by tidal pressure variations in the Clayoquot Slope at 1250 m may contribute to plume activation, but cannot explain the long duration increase in venting that were observed in response to hydrostatic pressure changes. Sultan et al. (2020) found evidence that gas exsolution from pore fluids does occur during low tides, but that this is not sufficient alone to trigger the release of gas in the water column at Arctic seeps on the Vestnesa Ridge. Our results concur with this latter finding as we could not relate the reactivation of quiescent vents to a particular tidal phase.

4.2.2 Non-periodic variability

Although a general tidal control is evident in our data, several gas emission peaks are not explained by the bottom pressure variations. Sudden ebullition events occasionally start during flood tide, although not as often as during ebb tide. The non-tidally-controlled ebullition events observed during the monitoring period could not be related to seismic vibrations or wave height variations. The broadband and short-period seismometers did not show any indication that the local seismicity contributed to the bubble release during our monitoring period. Neither the few high-amplitude short-duration bottom motion events nor the background low-amplitude ground-velocity variations could be linked with changes in the bubble release as monitored by SHROS and the cameras. Earthquakes are commonly cited as triggering mechanisms of gas seepage and venting (Field and Jennings, 1987; Hasiotis et al., 1996; Kuşçu et al., 2005; Mau et al., 2007; Obzhirov et al., 2004), even in gas-hydrate-bearing sediments (Fischer et al., 2013). Earthquakes can also be linked to pore pressure changes (Kopf et al., 2010). Our study found that the gas venting variability may not be related to the seismicity. Acoustic monitoring of the methane release in the Clayoquot Slope also found no relation between the gas venting activity and the seismicity (Römer et al., 2016). However, high frequency short duration events and long-lasting tremors have been linked to gas seepage (Tary et al., 2011; Franek et al., 2017; Tsang-Hin-Sun et al., 2019). Although we could not relate the high-amplitude SDEs with the bubble release, the SHROS has a bihourly sampling rate and we cannot fully exclude that SDEs or long-lasting seafloor tremors may be linked to the rise of bubbles through the subsurface. Swell-induced hydrostatic pressure variations could also influence the flux of bubble emissions. At shallow seeps near Coal Oil Point, Leifer and Boles (2005) showed that swell accounts for up to 4% and 0.9% of the bubble effluxes at respective water depths of 22 m and 200 m. SHR is significantly deeper and such influence would expectedly have much lower amplitude. In our data, the variations of the wave height data from the closest surface buoy across the monitoring period did not correlate with the variations of the bubble release.

As postulated by previous findings (Bangs et al., 2011; Kannberg et al., 2013; Philip et al., 2016a), it is clear that sediment permeability variations, which are unrelated to tidal loading and unloading cycles, also influence bubble release at SHR. Clogging caused by the formation of gas hydrates in fractures and pore spaces can decrease sediment permeability, leading to increased pore pressure (Bangs et al., 2011; Daigle et al., 2011; Daigle and Dugan, 2010; Tréhu et al., 2004a). Bangs et al. (2011) linked a temporary interruption of the venting at the SHR summit to an increase of gas build-up along Horizon A in the subsurface. Such pressure build-ups can open fractures through the GHSZ that propagate all the way to the surface through hydraulic fracturing (Bangs et al., 2011; Daigle and Dugan, 2010; Liu and Flemings, 2007; Tréhu et al., 2004a; Tryon et al., 2002). However, the timescales suggested for the gas build-up to reach sufficient pressures to overcome the overburden load are relatively long, years to decades (Bangs et al., 2011; Daigle et al., 2011), or even thousands of years (Daigle and Dugan, 2010). While we do not exclude that such long term venting phases occur at the scale of the whole SHR summit, the reported timescales (years) do not match with the short-term (few hours to few months) alternations of on/off periods that we observed at individual vents. The reactivation of vents after short quiescent phases implies that the pressures required to reopen pathways might be much lower than previously thought. Furthermore, the strong spatial variability in venting activity that was observed between the different vents, as well as between distinct bubble plumes within a same vent, is not reconcilable with a model in which fracture openings nucleate only from pressure build-up below the GHSZ. Our observations support a model in which the fracture nucleation is not restricted to the base of the GHSZ, but may also occur in shallower sediments (Daigle and Dugan, 2010b).

We argue that the bubble release is regulated by localized and shallow sub-bottom changes in hydraulic conductivity of the sediments that result in temporary accumulation of pockets of free gas within the GHSZ. Free gas within the GHSZ can be stable at SHR due to increased salinity and low sediment permeability, which restricts water availability in the sediments (Haeckel et al., 2004; Lee and Collett, 2006; Liu and Flemings, 2006; Tréhu et al., 2004a). By trapping free gas near the sediment surface, low sediment permeability or shallow blockages could cause the pore gas pressure to increase until the pressure at the top of the gas column reaches the necessary threshold to break the seal or open new fractures to the surface (Hantschel and Kauerauf, 2009). High ebullition events tend to start suddenly with a gas outrush and to taper off progressively. This is consistent with the sudden release of trapped, pressurized gas as a trigger for the onset of plumes and high ebullition events. Following the initial outburst, the bubble release decreases progressively over time as a result of decreasing pore gas pressure and ensuing constriction of the flow conduits. Consequently, the passage of methane decreases leading to a pressure increase in the gas column below the shallow bottleneck. The gas pressure increase within the pores may be enhanced by pumping due to hydrostatic loading and unloading cycles. One hypothesis would be that, because of the plastic behavior of gas cavities (Sills et al., 1991; Wheeler, 1990), cavities compressed during repeated loading cycles do not expand back during unloading phases, thus causing the gas pressure to increase gradually. The gas pressure required to overcome the vertical stress in such a scenario is much lower than the pressure necessary to nucleate or dilate fractures all the way from the bottom of the GHSZ. In 1999, scientists on board the DSV Alvin observed the release of large quantities of free methane gas that was previously trapped beneath a hydrate seal (Torres et al., 1999). Therefore, we posit that changes at the seabed surface such as those observed at the main vents with the cameras (sediment collapse, etc.) or shallow hydrate formation could cause blockages in the sediments and contribute to the variability of the gas release over short timescales of hours to days. The formation of hydrate from free gas can indeed be very rapid (Torres et al., 1999; Haeckel et al., 2004; Sultan et al., 2020), especially in shallow sediments (Tryon et al., 2002; Santos et al., 2012; Sultan et al., 2014) where the salinity is lower due to better seawater circulation (Colbert and Hammond, 2008).

Periphery sites with low activity may be supplied by lower gas fluxes from the feeder horizon, leading to longer pressure build-up times than the main vents. Alternatively, periphery sites might act as pressure relieving valves for the SHR summit that activate or deactivate following fluctuations of the gas pressure below the base of the GHSZ. The vents temporal variations showed a few conspicuous coordinated behaviors, especially between Smokey Tavern and Summit-D. Smokey Tavern was one of the most consistently active sites on the SHR summit. A cessation of venting at Smokey Tavern could cause a pressure increase at depths that would trigger an increase in activity at other vents. However, our data are not sufficient to prove whether the activity of the different sites is coordinated or merely coincidental. Longer data timeseries showing the relative variations of the different vents are needed to test this hypothesis.

The release of trapped free gas may also be aided by the strong bottom currents that we observed with the ADCP. The bottom currents might scour the shallow hydrates promoting their dissolution (Thomsen et al., 2012), potentially weakening hydrate blockages. Morphological highs on Oregon's continental shelf cause turbulent flow and enhanced form drag at the seabed (Nash and Moum, 2001), which can cause pressure and velocity fluctuations that affect the sediment pore system (Higashino et al., 2009). Strong bottom currents can also cause shear stress on sediments and facilitate plume onset from the just beneath the sediment where gas buoyancy alone would not have sufficed to trigger ebullition (Joyce and Jewell, 2003).

4.3 Bubble-induced upwelling flows

The ADCP timeseries shows that strong upwelling flows with minute-averaged upward velocities often exceeding 10-15 cm/s periodically occur in the bottom 250-300 m of the water column (Figure 9 and Dataset S2).

It is clear that the upwelling flows at SHR are caused by bubble venting activity. This is shown by the frequent co-occurrence in the ADCP of upwelling flows with bubble-induced data blanking. Gas bubbles rising in the water column can draw surrounding water into the rising plume, forming a local upwelling flow (Josenhans et al., 1978; Leifer et al., 2000; Leifer and Judd, 2002; Leifer and MacDonald, 2003; McGinnis et al., 2011; Milgram, 1983).

The upwelling flows recorded by the ADCP occurred at a semi-diurnal frequency and clearly during decreasing barotropic tidal phases. However, the SHROS results show that bubble release is reduced, but does not cease during rising tides. This indicates that upwelling flows should also vary in intensity, but not stop throughout the tidal cycles. Furthermore, the tidal control on bubble release rate observed with the SHROS is too weak to convey a strong semi-diurnal component to the upwelling velocities as was recorded by the ADCP. This contradiction results from a bias in the current velocity data caused by tidally-controlled horizontal currents that deflect the bubble plumes out of the acoustic beams of the ADCP during rising tide. The ADCP is located to the south and southeast of the main venting areas. The flow velocity data show that strong upwelling flows occur during times when the tidally-modulated dominant north-northwesterly current is weak or reversed (Figure 9).

The ADCP results indicate that most of the upwelling flows with velocities exceeding 5 cm/s rise up to a maximum of 300 m into the water column, corresponding to a depth of about

470 m. This is slightly above the upper limit of the gas hydrate stability zone (GHSZ), located ~490-510 m deep (Heeschen et al., 2003, 2005; Kannberg et al., 2013), which fits with the assumption that bubbles are protected by a hydrate-skin while rising through the GHSZ and dissolve rapidly after exiting the GHSZ (Heeschen et al., 2003; Rehder et al., 2002). Some upwelling flows could be traced above this depth and up to depths of 400-350 m. This is consistent with recent work using a ship echosounder that detected bubble plumes at the SHR summit up to a depth of 350 m (Philip et al., 2016a), indicating the persistence of some bubbles in the water column well above the top of the gas hydrate stability zone. It also supports the conjecture that upwelling flows cease when the rising bubbles dissolve (Leifer and Judd, 2002). The rise height of the bubble plumes may also vary seasonally because of water column stratification. Recent preliminary work on the ADCP data at SHR concluded that bubbles commonly rose up to the top 200 m of the water column, but this observation seems to be based on an erroneous depth scale in the ADCP data (Philip et al., 2016b) and it is not confirmed by our data.

5 Conclusions

Venting over the SHR summit is persistent and dynamic. It is evident that variations in plume activity at a single vent do not reflect variations of the total bubble release at the summit of SHR. Methane ebullition occurs in several distinct vent areas that are shaped by the combination of slow, venting-induced erosion of the seafloor and punctuated by sudden violent gas expulsion events. While active gas emissions are modulated by tidal loading and unloading cycles, there is evidence that local hydraulic conductivity changes at the sediment surface or in the shallow subsurface play a major role in controlling the short-term variability of gas release and impart a stochastic, non-periodic component to it. This may explain why previous work, based on less systematic sampling, could not ascertain correlations between methane release and the barotropic tidal cycles at SHR.

Onsets of plume formation and high ebullition events are facilitated during decreasing and low tidal pressures. However, our data showed that release of plumes with high bubble concentration can also occur at any point of the tidal cycle, which suggests that it is controlled by increasing gas pressure within the sediment pores rather than by decreasing hydrostatic loads. Based on our conclusions, a static increase in hydrostatic pressure (e.g. sea level rise), would only shift the thresholds for plume activation and deactivation, temporary delaying the pressure outbursts, but would not lead to a long-term reduction in methane ebullition.

Our results showed a strong temporal variability of the gas emissions, where a single vent can be found inactive, strongly active or anywhere between these two states depending on the time of observation. At SHR, the main vents were inactive 25% to about 50% of the time, and when these vents were active the plumes varied considerably in intensity. Hence, mean flux measurements should ideally be conducted over monitoring intervals that span several tidal cycles to minimize flux estimation errors due to temporal variability.

In addition, there is also a strong spatial variability between individual vents. Single plumes within an individual vent display strikingly different ebullition behaviors, clearly corresponding to different fluxes. In our data, it is evident that no single plume can be considered representative of the methane release dynamics of a vent area, and that no vent area is representative of the bubble release at the scale of the SHR summit. Hence, flux estimations for the SHR summit should not rely on single vent monitoring and should take spatial variability of the bubble release into consideration by focusing on several of the main vent areas.

Because of the scarcity of flux data available and the challenges posed by measuring methane fluxes at the seafloor, global estimates often rely on spatial and temporal extrapolation of local, short-duration measurements (Weber et al., 2019). Although we are not able to quantify the fluxes with our sonar data, to assume that the venting activity of a main vent is representative of the general venting activity at the SHR summit might lead to overestimations or underestimations potentially up to several orders of magnitudes (depending on the status of the vent observed at the time of monitoring, and that of those not observed). Extrapolating such estimates to even larger spatial and temporal scales (e.g. global estimates) would likely magnify these errors even further, as SHR may not be representative of an "average seep" in terms of venting activity. In this regard, the current global flux estimates could actually be less reliable than previously thought.

This work shows that systematic monitoring of one plume, or a single vent, results in a very incomplete understanding of the venting dynamics of the whole system. Furthermore, it illustrates the value of underwater cabled observatories by providing timeseries data collected systematically by an array of instruments and sensors, allowing detailed examination of process linkages yielding a comprehensive understanding of the study area. The acoustic monitoring, combined with in-situ CTD data, camera observations and 3D-photomosaic, was essential to comprehend the short-term variability and the spatial distribution of the venting activity over the entire summit.

Acknowledgments

We thank the University of Washington OOI Regional Cabled Array team and the captains and crew of R/V *Roger Revelle* and R/V *Atlantis* for their invaluable assistance during the VISIONS'18 and VISIONS'19 expeditions. The 3D mosaic data used in this work were collected using the AUV AE2000f during the Schmidt Ocean Institute's FK180731 #Adaptive Robotics campaign. We thank the crew of the R/V *Falkor* and in particular Kazunori Nagano and Tetsu Koike (University of Tokyo) for the AUV operations. We also thank the two anonymous reviewers for their constructive reviews of the manuscript. This work is supported by the German Federal Ministry of Education and Research (BMBF) under the grant numbers 03F0765A and 03F0854A and is based upon work supported by the National Science Foundation under Cooperative Agreement No. 1743430 (which supports the OOI).

Data

Data from the SHROS (OVRSRA101), scanning- sonar (QNTSRA101), 4K camera (CAMPIA101), and CTD probe (CTDPFA110) instruments are available on the _University of Washington webserver for PI-added instruments (http://piweb.ooirsn.uw.edu/marum/data/). Original CAMDSB103 still photographs can be downloaded from the OOI Raw Data Archive (direct link: https://rawdata-west.oceanobservatories.org/files/RS01SUM2/MJ01B/05-CAMDSB103/). Data from the other cabled instruments can be downloaded from the OOI website (https://oceanobservatories.org/instruments/), the OOI Data Portal (https://ooinet.oceanobservatories.org/) and the OOI Raw Data Archive (https://rawdata.oceanobservatories.org/). Seismic data from the ocean bottom seismometers (OBS) is available from the IRIS Data Management Center (www.iris.edu). Wave height data from the surface buoys can be downloaded from the National Data Buoy Center of the National Oceanographic and Atmospheric Administration (https://www.ndbc.noaa.gov/).

References

Ainslie, M.A., McColm, J.G., 1998. A simplified formula for viscous and chemical absorption in sea water. J. Acoust. Soc. Am. 103, 1671–1672. https://doi.org/10.1121/1.421258

Bangs, N.L.B., Hornbach, M.J., Berndt, C., 2011. The mechanics of intermittent methane venting at South Hydrate Ridge inferred from 4D seismic surveying. Earth Planet. Sci. Lett. 310, 105–112. https://doi.org/10.1016/j.epsl.2011.06.022

Bayrakci, G., Scalabrin, C., Dupré, S., Leblond, I., Tary, J.-B., Lanteri, N., Augustin, J.-M., Berger, L., Cros, E., Ogor, A., Tsabaris, C., Lescanne, M., Géli, L., 2014. Acoustic monitoring of gas emissions from the seafloor. Part II: a case study from the Sea of Marmara. Mar. Geophys. Res. 35, 211–229. https://doi.org/10.1007/s11001-014-9227-7

Berndt, C., Feseker, T., Treude, T., Krastel, S., Liebetrau, V., Niemann, H., Bertics, V.J., Dumke, I., Dünnbier, K., Ferré, B., Graves, C., Gross, F., Hissmann, K., Hühnerbach, V., Krause, S., Lieser, K., Schauer, J., Steinle, L., 2014. Temporal Constraints on Hydrate-Controlled Methane Seepage off Svalbard. Science 343, 284–287. https://doi.org/10.1126/science.1246298

Boetius, A., Suess, E., 2004. Hydrate Ridge: a natural laboratory for the study of microbial life fueled by methane from near-surface gas hydrates. Chem. Geol., Geomicrobiology and Biogeochemistry of Gas Hydrates and Hydrocarbon Seeps 205, 291–310. https://doi.org/10.1016/j.chemgeo.2003.12.034

Bohrmann, G., Blinova, V., Dehning, K., Evtushenko, D., Friese, C., Hiruta, A., Hüttich, D., Ivanov, M., Klapp, S.A., Körber, J.H., Komakhidze, G., Kopiske, E., Lange, K., Mai, H.A., Malakhova, T., Marcon, Y., Meinecke, G., Pape, T., Ratmeyer, V., Rehage, R., Renken, J., Reuter, C., Reuter, M., Römer, M., Sahling, H., Sakvarelidze, E., Wintersteller, P., Zarrouk, M., 2011. Report and preliminary results of RV MARIA S. MERIAN Cruise MSM 15/2, Istanbul (Turkey) - Piraeus (Greece), 10 May - 2 June 2010. Origin and structure of methane, gas hydrates and fluid flows in the Black Sea. (Cruise report No. 278), Berichte aus dem Fachbereich Geowissenschaften. Geowissenschaften, Universität Bremen, Bremen.

Bohrmann, G., Greinert, J., Suess, E., Torres, M., 1998. Authigenic carbonates from the Cascadia subduction zone and their relation to gas hydrate stability. Geology 26, 647–650. https://doi.org/10.1130/0091-7613(1998)026<0647:ACFTCS>2.3.CO;2

Boles, J.R., Clark, J.F., Leifer, I., Washburn, L., 2001. Temporal variation in natural methane seep rate due to tides, Coal Oil Point area, California. J. Geophys. Res. Oceans 106, 27077–27086. https://doi.org/10.1029/2000JC000774

Colbert, S.L., Hammond, D.E., 2008. Shoreline and seafloor fluxes of water and short-lived Ra isotopes to surface water of San Pedro Bay, CA. Mar. Chem. 108, 1–17. https://doi.org/10.1016/j.marchem.2007.09.004

Daigle, H., Bangs, N.L., Dugan, B., 2011. Transient hydraulic fracturing and gas release in methane hydrate settings: A case study from southern Hydrate Ridge. Geochem. Geophys. Geosystems 12. https://doi.org/10.1029/2011GC003841

Daigle, H., Dugan, B., 2010. Origin and evolution of fracture-hosted methane hydrate deposits. J. Geophys. Res. Solid Earth 115. https://doi.org/10.1029/2010JB007492

Ferré, B., Jansson, P.G., Moser, M., Serov, P., Portnov, A., Graves, C.A., Panieri, G., Gründger, F., Berndt, C., Lehmann, M.F., Niemann, H., 2020. Reduced methane seepage from Arctic sediments during cold bottom-water conditions. Nat. Geosci. 13, 144–148. https://doi.org/10.1038/s41561-019-0515-3

Field, M.E., Jennings, A.E., 1987. Seafloor gas seeps triggered by a northern California earthquake. Mar. Geol. 77, 39–51. https://doi.org/10.1016/0025-3227(87)90082-X

Fischer, D., Mogollón, J.M., Strasser, M., Pape, T., Bohrmann, G., Fekete, N., Spiess, V., Kasten, S., 2013. Subduction zone earthquake as potential trigger of submarine hydrocarbon seepage. Nat. Geosci. 6, 647–651. https://doi.org/10.1038/ngeo1886

Franek, P., Plaza-Faverola, A., Mienert, J., Buenz, S., Ferré, B., Hubbard, A., 2017. Microseismicity Linked to Gas Migration and Leakage on the Western Svalbard Shelf. Geochem. Geophys. Geosystems 18, 4623–4645. https://doi.org/10.1002/2017GC007107

Greinert, J., 2008. Monitoring temporal variability of bubble release at seeps: The hydroacoustic swath system GasQuant. J. Geophys. Res. Oceans 113. https://doi.org/10.1029/2007JC004704

Greinert, J., Artemov, Y., Egorov, V., De Batist, M., McGinnis, D., 2006. 1300-m-high rising bubbles from mud volcanoes at 2080 m in the Black Sea: Hydroacoustic characteristics and temporal variability. Earth Planet. Sci. Lett. 244, 1–15. https://doi.org/doi: DOI: 10.1016/j.epsl.2006.02.011

Haeckel, M., Suess, E., Wallmann, K., Rickert, D., 2004. Rising methane gas bubbles form massive hydrate layers at the seafloor. Geochim. Cosmochim. Acta 68, 4335–4345. https://doi.org/10.1016/j.gca.2004.01.018

Hantschel, T., Kauerauf, A.I., 2009. Pore Pressure, Compaction and Tectonics, in: Fundamentals of Basin and Petroleum Systems Modeling. Springer, Berlin, Heidelberg, pp. 31–101. https://doi.org/10.1007/978-3-540-72318-9_2

Hasiotis, T., Papatheodorou, G., Kastanos, N., Ferentinos, G., 1996. A pockmark field in the Patras Gulf (Greece) and its activation during the 14/7/93 seismic event. Mar. Geol. 130, 333–344. https://doi.org/10.1016/0025-3227(95)00131-X

Hautala, S.L., Solomon, E.A., Johnson, H.P., Harris, R.N., Miller, U.K., 2014. Dissociation of Cascadia margin gas hydrates in response to contemporary ocean warming. Geophys. Res. Lett. 41, 8486–8494. https://doi.org/10.1002/2014GL061606

Heeschen, K.U., Collier, R.W., de Angelis, M.A., Suess, E., Rehder, G., Linke, P., Klinkhammer, G.P., 2005. Methane sources, distributions, and fluxes from cold vent sites at Hydrate Ridge, Cascadia Margin. Glob. Biogeochem. Cycles 19. https://doi.org/10.1029/2004GB002266

Heeschen, K.U., Tréhu, A.M., Collier, R.W., Suess, E., Rehder, G., 2003. Distribution and height of methane bubble plumes on the Cascadia Margin characterized by acoustic imaging. Geophys. Res. Lett. 30. https://doi.org/10.1029/2003GL016974

Higashino, M., Clark, J.J., Stefan, H.G., 2009. Pore water flow due to near-bed turbulence and associated solute transfer in a stream or lake sediment bed. Water Resour. Res. 45. https://doi.org/10.1029/2008WR007374

Hilmo, R., Wilcock, W.S.D., 2020. Physical Sources of High-Frequency Seismic Noise on Cascadia Initiative Ocean Bottom Seismometers. Geochem. Geophys. Geosystems 21, e2020GC009085. https://doi.org/10.1029/2020GC009085

Holzner, C.P., McGinnis, D.F., Schubert, C.J., Kipfer, R., Imboden, D.M., 2008. Noble gas anomalies related to high-intensity methane gas seeps in the Black Sea. Earth Planet. Sci. Lett. 265, 396–409. https://doi.org/10.1016/j.epsl.2007.10.029

IPCC, 2013. Climate Change 2013: The Physical Science Basis. Contribution of Working Group I to the Fifth Assessment Report of the Intergovernmental Panel on Climate Change (IPCC Assessment Report No. AR5). IPCC, Cambridge, United Kingdom and New York, NY, USA.

Jackson, D.R., Williams, K.L., Wever, T.F., Friedrichs, C.T., Wright, L.D., 1998. Sonar evidence for methane ebullition in Eckernförde Bay. Cont. Shelf Res. 18, 1893–1915. https://doi.org/10.1016/S0278-4343(98)00062-4

Johansen, C., Todd, A.C., MacDonald, I.R., 2017. Time series video analysis of bubble release processes at natural hydrocarbon seeps in the Northern Gulf of Mexico. Mar. Pet. Geol. 82, 21–34. https://doi.org/10.1016/j.marpetgeo.2017.01.014

Johnson-Roberson, M., Pizarro, O., Willams, S., 2009. Towards large scale optical and acoustic sensor integration for visualization, in: Proceedings of the MTS/IEEE Oceans 2009 Conference. pp. 1–4.

Josenhans, H.W., King, L.H., Fader, G.B., 1978. A side-scan sonar mosaic of pockmarks on the Scotian Shelf. Can. J. Earth Sci. 15, 831–840. https://doi.org/10.1139/e78-088

Joyce, J., Jewell, P.W., 2003. Physical Controls on Methane Ebullition from Reservoirs and Lakes. Environ. Eng. Geosci. 9, 167–178. https://doi.org/10.2113/9.2.167

Kannberg, P.K., Tréhu, A.M., Pierce, S.D., Paull, C.K., Caress, D.W., 2013. Temporal variation of methane flares in the ocean above Hydrate Ridge, Oregon. Earth Planet. Sci. Lett. 368, 33–42. https://doi.org/10.1016/j.epsl.2013.02.030

Kopf, A., Delisle, G., Faber, E., Panahi, B., Aliyev, C.S., Guliyev, I., 2010. Long-term in situ monitoring at Dashgil mud volcano, Azerbaijan: a link between seismicity, pore-pressure transients and methane emission. Int. J. Earth Sci. 99, 227–240. https://doi.org/10.1007/s00531-009-0487-4

Körber, J.-H., Sahling, H., Pape, T., dos Santos Ferreira, C., MacDonald, I., Bohrmann, G., 2014. Natural oil seepage at Kobuleti Ridge, eastern Black Sea. Mar. Pet. Geol. 50, 68–82. https://doi.org/10.1016/j.marpetgeo.2013.11.007

Kumar, D., Sen, M.K., Bangs, N.L., 2006. Seismic characteristics of gas hydrates at Hydrate Ridge, offshore Oregon. Lead. Edge 25, 610–614. https://doi.org/10.1190/1.2202665

Kuşçu, İ., Okamura, M., Matsuoka, H., Gökaşan, E., Awata, Y., Tur, H., Şimşek, M., Keçer, M., 2005. Seafloor gas seeps and sediment failures triggered by the August 17, 1999 earthquake in the Eastern part of the Gulf of İzmit, Sea of Marmara, NW Turkey. Mar. Geol. 215, 193–214. https://doi.org/10.1016/j.margeo.2004.12.002

Kvenvolden, K.A., Lorenson, T.D., 2001. The Global Occurrence of Natural Gas Hydrate, in: Paull, C.K., Dillon, W.P. (Eds.), Natural Gas Hydrates: Occurrence, Distribution, and Detection, Geophysical Monograph. American Geophysical Union (AGU), pp. 3–18. https://doi.org/10.1029/GM124p0003

Kvenvolden, K.A., Rogers, B.W., 2005. Gaia's breath—global methane exhalations. Mar. Pet. Geol., Near-Surface Hydrocarbon Migration: Mechanisms and Seepage Rates 22, 579–590. https://doi.org/10.1016/j.marpetgeo.2004.08.004

Lee, M.W., Collett, T.S., 2006. Ocean Drilling Program Leg 204 Scientific Results: Gas Hydrate and Free Gas Saturations Estimated from Velocity Logs on Hydrate Ridge, Offshore Oregon, USA, in: Tréhu, A.M., Bohrmann, G., Torres, M.E., Colwell, F.S. (Eds.), Proceedings of the Ocean Drilling Program. Scientific Results. College Station, TX (Ocean Drilling Program), pp. 1–25. https://doi.org/10.2973/odp.proc.sr.204.114.2006

Leifer, I., Boles, J., 2005. Turbine tent measurements of marine hydrocarbon seeps on subhourly timescales. J. Geophys. Res. Oceans 110. https://doi.org/10.1029/2003JC002207

Leifer, I., Clark, J.F., Chen, R.F., 2000. Modifications of the local environment by natural marine hydrocarbon seeps. Geophys. Res. Lett. 27, 3711–3714. https://doi.org/10.1029/2000GL011619

Leifer, I., Judd, A.G., 2002. Oceanic methane layers: the hydrocarbon seep bubble deposition hypothesis. Terra Nova 14, 417–424. https://doi.org/10.1046/j.1365-3121.2002.00442.x

Leifer, I., MacDonald, I., 2003. Dynamics of the gas flux from shallow gas hydrate deposits: interaction between oily hydrate bubbles and the oceanic environment. Earth Planet. Sci. Lett. 210, 411–424. https://doi.org/10.1016/S0012-821X(03)00173-0

Leifer, I., Patro, R.K., 2002. The bubble mechanism for methane transport from the shallow sea bed to the surface: A review and sensitivity study. Cont. Shelf Res., Gas in Marine Sediments: Contributions from the 5th International Conference orgainsed by the Shallow Gas Group, Bologna, Italy, September 1998 22, 2409–2428. https://doi.org/10.1016/S0278-4343(02)00065-1

Leonte, M., Kessler, J.D., Kellermann, M.Y., Arrington, E.C., Valentine, D.L., Sylva, S.P., 2017. Rapid rates of aerobic methane oxidation at the feather edge of gas hydrate stability in the waters of Hudson Canyon, US Atlantic Margin. Geochim. Cosmochim. Acta 204, 375–387. https://doi.org/10.1016/j.gca.2017.01.009

Liu, X., Flemings, P., 2009. Dynamic response of oceanic hydrates to sea level drop. Geophys. Res. Lett. 36. https://doi.org/10.1029/2009GL039821

Liu, X., Flemings, P.B., 2007. Dynamic multiphase flow model of hydrate formation in marine sediments. J. Geophys. Res. Solid Earth 112. https://doi.org/10.1029/2005JB004227

Liu, X., Flemings, P.B., 2006. Passing gas through the hydrate stability zone at southern Hydrate Ridge, offshore Oregon. Earth Planet. Sci. Lett. 241, 211–226. https://doi.org/10.1016/j.epsl.2005.10.026

MacDonald, I.R., Leifer, I., Sassen, R., Stine, P., Mitchell, R., Guinasso, N., 2002. Transfer of hydrocarbons from natural seeps to the water column and atmosphere. Geofluids 2, 95–107. https://doi.org/10.1046/j.1468-8123.2002.00023.x

Maeck, A., Hofmann, H., Lorke, A., 2014. Pumping methane out of aquatic sediments – ebullition forcing mechanisms in an impounded river. Biogeosciences 11, 2925–2938. https://doi.org/10.5194/bg-11-2925-2014

Marcon, Y., Kopiske, E., Leymann, T., Spiesecke, U., Vittori, V., Wahl, T. von, Wintersteller, P., Waldmann, C., Bohrmann, G., 2019. A Rotary Sonar for Long-Term Acoustic Monitoring of Deep-Sea Gas Emissions, in: Proceedings of the IEEE/MTS OCEANS 2019 Conference. Presented at the OCEANS 2019 - Marseille, pp. 1–8. https://doi.org/10.1109/OCEANSE.2019.8867218

Martens, C.S., Val Klump, J., 1980. Biogeochemical cycling in an organic-rich coastal marine basin—I. Methane sediment-water exchange processes. Geochim. Cosmochim. Acta 44, 471–490. https://doi.org/10.1016/0016-7037(80)90045-9

Mau, S., Rehder, G., Arroyo, I.G., Gossler, J., Suess, E., 2007. Indications of a link between seismotectonics and CH4 release from seeps off Costa Rica. Geochem. Geophys. Geosystems 8. https://doi.org/10.1029/2006GC001326

Mau, S., Römer, M., Torres, M.E., Bussmann, I., Pape, T., Damm, E., Geprägs, P., Wintersteller, P., Hsu, C.-W., Loher, M., Bohrmann, G., 2017. Widespread methane seepage along the continental margin off Svalbard - from Bjørnøya to Kongsfjorden. Sci. Rep. 7, 42997. https://doi.org/10.1038/srep42997

McGinnis, D.F., Greinert, J., Artemov, Y., Beaubien, S.E., Wüest, A., 2006. Fate of rising methane bubbles in stratified waters: How much methane reaches the atmosphere? J. Geophys. Res. Oceans 111. https://doi.org/10.1029/2005JC003183

McGinnis, D.F., Schmidt, M., DelSontro, T., Themann, S., Rovelli, L., Reitz, A., Linke, P., 2011. Discovery of a natural CO2 seep in the German North Sea: Implications for shallow dissolved gas and seep detection. J. Geophys. Res. Oceans 116. https://doi.org/10.1029/2010JC006557

Merewether, R., Olsson, M.S., Lonsdale, P., 1985. Acoustically detected hydrocarbon plumes rising from 2-km depths in Guaymas Basin, Gulf of California. J. Geophys. Res. Solid Earth 90, 3075–3085. https://doi.org/10.1029/JB090iB04p03075

Milgram, J.H., 1983. Mean flow in round bubble plumes. J. Fluid Mech. 133, 345–376. https://doi.org/10.1017/S0022112083001950

Moszyński, M., Stepnowski, A., 2002. Time-varied-gain correction for digital echosounders. Presented at the Forum Acusticum, Sevilla.

Myhre, C.L., Ferré, B., Platt, S.M., Silyakova, A., Hermansen, O., Allen, G., Pisso, I., Schmidbauer, N., Stohl, A., Pitt, J., Jansson, P., Greinert, J., Percival, C., Fjaeraa, A.M., O'Shea, S.J., Gallagher, M., Breton, M.L., Bower, K.N., Bauguitte, S.J.B., Dalsøren, S., Vadakkepuliyambatta, S., Fisher, R.E., Nisbet, E.G., Lowry, D., Myhre, G., Pyle, J.A., Cain, M., Mienert, J., 2016. Extensive release of methane from Arctic seabed west of Svalbard during summer 2014 does not influence the atmosphere. Geophys. Res. Lett. 43, 4624–4631. https://doi.org/10.1002/2016GL068999

Nash, J.D., Moum, J.N., 2001. Internal hydraulic flows on the continental shelf: High drag states over a small bank. J. Geophys. Res. Oceans 106, 4593–4611. https://doi.org/10.1029/1999JC000183

Obzhirov, A., Shakirov, R., Salyuk, A., Suess, E., Biebow, N., Salomatin, A., 2004. Relations between methane venting, geological structure and seismo-tectonics in the Okhotsk Sea. Geo-Mar. Lett. 24, 135–139. https://doi.org/10.1007/s00367-004-0175-0

Pape, T., Bahr, A., Klapp, S.A., Abegg, F., Bohrmann, G., 2011. High-intensity gas seepage causes rafting of shallow gas hydrates in the southeastern Black Sea. Earth Planet. Sci. Lett. 307, 35–46. https://doi.org/10.1016/j.epsl.2011.04.030

Paull, C.K., Brewer, P.G., Ussler, W., Peltzer, E.T., Rehder, G., Clague, D., 2003. An experiment demonstrating that marine slumping is a mechanism to transfer methane from seafloor gas-hydrate deposits into the upper ocean and atmosphere. Geo-Mar. Lett. 22, 198–203. https://doi.org/10.1007/s00367-002-0113-y

Paull, C.K., Normark, W.R., Ussler, W., Caress, D.W., Keaten, R., 2008. Association among active seafloor deformation, mound formation, and gas hydrate growth and accumulation within the seafloor of the Santa Monica Basin, offshore California. Mar. Geol. 250, 258–275. https://doi.org/10.1016/j.margeo.2008.01.011

Paull, C.K., Ussler, W., Borowski, W.S., Spiess, F.N., 1995. Methane-rich plumes on the Carolina continental rise: Associations with gas hydrates. Geology 23, 89–92. https://doi.org/10.1130/0091-7613(1995)023<0089:MRPOTC>2.3.CO;2

Philip, B.T., Denny, A.R., Solomon, E.A., Kelley, D.S., 2016a. Time-series measurements of bubble plume variability and water column methane distribution above Southern Hydrate Ridge, Oregon. Geochem. Geophys. Geosystems 17, 1182–1196. https://doi.org/10.1002/2016GC006250

Philip, B.T., Kelley, D.S., Solomon, E.A., Delaney, J.R., 2016b. Monitoring methane emissions at Southern Hydrate Ridge using an OOI Cabled Array Acoustic Doppler Current Profiler. Presented at the OCEANS 2016 MTS/IEEE Monterey, IEEE, Monterey, CA, USA, pp. 1–5. https://doi.org/10.1109/OCEANS.2016.7761469

Rehder, G., Brewer, P.W., Peltzer, E.T., Friederich, G., 2002. Enhanced lifetime of methane bubble streams within the deep ocean. Geophys. Res. Lett. 29, 21-1-21–4. https://doi.org/10.1029/2001GL013966

Rehder, G., Leifer, I., Brewer, P.G., Friederich, G., Peltzer, E.T., 2009. Controls on methane bubble dissolution inside and outside the hydrate stability field from open ocean field experiments and numerical modeling. Mar. Chem. 114, 19–30. https://doi.org/10.1016/j.marchem.2009.03.004

Römer, M., Hsu, C.-W., Loher, M., MacDonald, I.R., dos Santos Ferreira, C., Pape, T., Mau, S., Bohrmann, G., Sahling, H., 2019. Amount and Fate of Gas and Oil Discharged at 3400 m Water Depth From a Natural Seep Site in the Southern Gulf of Mexico. Front. Mar. Sci. 6. https://doi.org/10.3389/fmars.2019.00700

Römer, M., Riedel, M., Scherwath, M., Heesemann, M., Spence, G.D., 2016. Tidally controlled gas bubble emissions: A comprehensive study using long-term monitoring data from the NEPTUNE cabled observatory offshore Vancouver Island. Geochem. Geophys. Geosystems 17, 3797–3814. https://doi.org/10.1002/2016GC006528

Römer, M., Sahling, H., Pape, T., Bahr, A., Feseker, T., Wintersteller, P., Bohrmann, G., 2012. Geological control and magnitude of methane ebullition from a high-flux seep area in the Black Sea—the Kerch seep area. Mar. Geol. 319–322, 57–74. https://doi.org/10.1016/j.margeo.2012.07.005

Sahling, H., Ahrlich, F., Bohrmann, G., Borowski, C., Breitzke, M., Buchheister, S., Büttner, H., Ferreira, C., Gaytán-Caballero, A., Geprägs, P., Groeneveld, J.-D., Hsu, C.-W., Jiménez-Guadarrama, E., Klar, S., Klaucke, I., Klüber, S., Leymann, T., Loher, M., Mai, H.-A., Mau, S., MacDonald, I., Marcon, Y., Meinecke, G., Melcher, A.-C., Morales-Dominguez, E., Raeke, A., Rehage, R., Renken, J., Reuter, M., Rohleder, C., Römer, M., Rubin-Blum, M., Schade, T., Schubotz, F., Seiter, C., Smrzka, D., Spiesecke, U., Torres, M., Vittori, V., VonNeuhoff, S., von Wahl, T., Wegener, G., Wiebe, M., Wintersteller, P., Zarrouk, M., Zwicker, J., 2017. R/V METEOR Cruise Report M114, Natural hydrocarbon seepage in the southern Gulf of Mexico, Kingston - Kingston, 12 February - 28 March 2015 (Cruise report No. 315), Berichte aus dem MARUM und dem Fachbereich Geowissenschaften der Universität Bremen. MARUM – Zentrum für Marine Umweltwissenschaften, Fachbereich Geowissenschaften, Universität Bremen, Bremen.

Santos, I.R., Eyre, B.D., Huettel, M., 2012. The driving forces of porewater and groundwater flow in permeable coastal sediments: A review. Estuar. Coast. Shelf Sci. 98, 1–15. https://doi.org/10.1016/j.ecss.2011.10.024

Saunois, M., Stavert, A.R., Poulter, B., Bousquet, P., Canadell, J.G., Jackson, R.B., Raymond, P.A., Dlugokencky, E.J., Houweling, S., Patra, P.K., Ciais, P., Arora, V.K., Bastviken, D., Bergamaschi, P., Blake, D.R., Brailsford, G., Bruhwiler, L., Carlson, K.M., Carrol, M., Castaldi, S., Chandra, N., Crevoisier, C., Crill, P.M., Covey, K., Curry, C.L., Etiope, G., Frankenberg, C., Gedney, N., Hegglin, M.I., Höglund-Isaksson, L., Hugelius, G., Ishizawa, M., Ito, A., Janssens-Maenhout, G., Jensen, K.M., Joos, F., Kleinen, T., Krummel, P.B., Langenfelds, R.L., Laruelle, G.G., Liu, L., Machida, T., Maksyutov, S., McDonald, K.C., McNorton, J., Miller, P.A., Melton, J.R., Morino, I., Müller, J., Murguia-Flores, F., Naik, V., Niwa, Y., Noce, S., O'Doherty, S., Parker, R.J., Peng, C., Peng, S., Peters, G.P., Prigent, C., Prinn, R., Ramonet, M., Regnier, P., Riley, W.J., Rosentreter, J.A., Segers, A., Simpson, I.J., Shi, H., Smith, S.J., Steele, L.P., Thornton, B.F., Tian, H., Tohjima, Y., Tubiello, F.N., Tsuruta, A., Viovy, N., Voulgarakis, A., Weber, T.S., van Weele, M., van der Werf, G.R., Weiss, R.F., Worthy, D., Wunch, D., Yin, Y., Yoshida, Y., Zhang, W., Zhang, Z., Zhao, Y., Zheng, B., Zhu, Qing, Zhu, Qiuan, Zhuang, Q., 2020. The Global Methane Budget 2000–2017. Earth Syst. Sci. Data 12, 1561–1623. https://doi.org/10.5194/essd-12-1561-2020

SBE Application Note No. 6, 2004. Determination of Sound Velocity from CTD Data (Application Note No. 6). SBE Sea-Bird Electronics, Inc., 13431 NE 20th Street, Bellevue, WA 98005, USA.

Scandella, B.P., Varadharajan, C., Hemond, H.F., Ruppel, C., Juanes, R., 2011. A conduit dilation model of methane venting from lake sediments. Geophys. Res. Lett. 38. https://doi.org/10.1029/2011GL046768

Schneider von Deimling, J., Greinert, J., Chapman, N.R., Rabbel, W., Linke, P., 2010. Acoustic imaging of natural gas seepage in the North Sea: Sensing bubbles controlled by variable currents. Limnol. Oceanogr. Methods 8, 155–171. https://doi.org/10.4319/lom.2010.8.155

Serié, C., Huuse, M., Schødt, N.H., 2012. Gas hydrate pingoes: Deep seafloor evidence of focused fluid flow on continental margins. Geology 40, 207–210. https://doi.org/10.1130/G32690.1

Shitashima, K., Maeda, Y., Koike, Y., Ohsumi, T., 2008. Natural analogue of the rise and dissolution of liquid CO2 in the ocean. Int. J. Greenh. Gas Control 2, 95–104. https://doi.org/10.1016/S1750-5836(07)00092-8

Sills, G.C., Wheeler, S.J., Thomas, S.D., Gardner, T.N., 1991. Behaviour of offshore soils containing gas bubbles. Géotechnique 41, 227–241. https://doi.org/10.1680/geot.1991.41.2.227

Silyakova, A., Jansson, P., Serov, P., Ferré, B., Pavlov, A.K., Hattermann, T., Graves, C.A., Platt, S.M., Myhre, C.L., Gründger, F., Niemann, H., 2020. Physical controls of dynamics of methane venting from a shallow seep area west of Svalbard. Cont. Shelf Res. 194, 104030. https://doi.org/10.1016/j.csr.2019.104030

Stepnowski, A., Mitchell, R.S., 1990. ECOLOG II: a real-time acoustic signal processing system for fish stock assessment. Ultrasonics 28, 256–265. https://doi.org/10.1016/0041-624X(90)90092-3

Suess, E., Torres, M., Bohrmann, G., Collier, R., Rickert, D., Goldfinger, C., Linke, P., Heuser, A., Sahling, H., Heeschen, K., Jung, C., Nakamura, K., Greinert, J., Pfannkuche, O., Trehu, A., Klinkhammer, G., Whiticar, M., Eisenhauer, A., Teichert, B., Elver, M., 2001. Sea floor methane hydrates at Hydrate Ridge, Cascadia margin, in: Natural Gas Hydrates: Occurrence, Distribution, and Detection, Geophysical Monograph Series. Washington, D.C., pp. 87–98.

Sultan, N., Bohrmann, G., Ruffine, L., Pape, T., Riboulot, V., Colliat, J.-L., Prunelé, A.D., Dennielou, B., Garziglia, S., Himmler, T., Marsset, T., Peters, C.A., Rabiu, A., Wei, J., 2014. Pockmark formation and evolution in deep water Nigeria: Rapid hydrate growth versus slow hydrate dissolution. J. Geophys. Res. Solid Earth 119, 2679–2694. https://doi.org/10.1002/2013JB010546

Sultan, N., Marsset, B., Ker, S., Marsset, T., Voisset, M., Vernant, A.M., Bayon, G., Cauquil, E., Adamy, J., Colliat, J.L., Drapeau, D., 2010. Hydrate dissolution as a potential mechanism for pockmark formation in the Niger delta. J. Geophys. Res. Solid Earth 115. https://doi.org/10.1029/2010JB007453

Sultan, N., Plaza-Faverola, A., Vadakkepuliyambatta, S., Buenz, S., Knies, J., 2020. Impact of tides and sea-level on deep-sea Arctic methane emissions. Nat. Commun. 11, 5087. https://doi.org/10.1038/s41467-020-18899-3

Tary, J.B., Géli, L., Henry, P., Natalin, B., Gasperini, L., Çomoğlu, M., Çağatay, N., Bardainne, T., 2011. Sea-Bottom Observations from the Western Escarpment of the Sea of Marmara. Bull. Seismol. Soc. Am. 101, 775–791. https://doi.org/10.1785/0120100014

Thomsen, L., Barnes, C., Best, M., Chapman, R., Pirenne, B., Thomson, R., Vogt, J., 2012. Ocean circulation promotes methane release from gas hydrate outcrops at the NEPTUNE Canada Barkley Canyon node. Geophys. Res. Lett. 39. https://doi.org/10.1029/2012GL052462

Thornton, B., Bodenmann, A., Pizarro, O., Williams, S.B., Friedman, A., Nakajima, R., Takai, K., Motoki, K., Watsuji, T., Hirayama, H., Matsui, Y., Watanabe, H., Ura, T., 2016. Biometric assessment of deep-sea vent megabenthic communities using multi-resolution 3D image reconstructions. Deep Sea Res. Part Oceanogr. Res. Pap. 116, 200–219. https://doi.org/10.1016/j.dsr.2016.08.009

Torres, M.E., Bohrmann, G., Brown, K., deAngelis, M., Hammond, D.E., Klinkhammer, G.P., McManus, J., Suess, E., Tréhu, A.M., 1999. Geochemical observations on Hydrate Ridge, Cascadia Margin during RV-ATLANTIS-cruise AT3-35b,.

Torres, M.E., McManus, J., Hammond, D.E., de Angelis, M.A., Heeschen, K.U., Colbert, S.L., Tryon, M.D., Brown, K.M., Suess, E., 2002. Fluid and chemical fluxes in and out of sediments hosting methane hydrate deposits on Hydrate Ridge, OR, I: Hydrological provinces. Earth Planet. Sci. Lett. 201, 525–540. https://doi.org/10.1016/S0012-821X(02)00733-1

Tréhu, A.M., 2006. Ocean Drilling Program Leg 204 Scientific Results: Subsurface Temperatures beneath Southern Hydrate Ridge, in: Tréhu, A.M., Bohrmann, G., Torres, M.E., Colwell, F.S. (Eds.), Proceedings of the Ocean Drilling Program. Scientific Results. College Station, TX (Ocean Drilling Program), pp. 1–26. https://doi.org/10.2973/odp.proc.sr.204.114.2006

Tréhu, A.M., Bohrmann, G., Rack, F.R., Torres, M.E., et al. (Eds.), 2003. Proceedings of the Ocean Drilling Program, 204 Initial Reports, Proceedings of the Ocean Drilling Program. Ocean Drilling Program. https://doi.org/10.2973/odp.proc.ir.204.2003

Tréhu, A.M., Flemings, P.B., Bangs, N.L., Chevallier, J., Gràcia, E., Johnson, J.E., Liu, C.-S., Liu, X., Riedel, M., Torres, M.E., 2004a. Feeding methane vents and gas hydrate deposits at south Hydrate Ridge. Geophys. Res. Lett. 31. https://doi.org/10.1029/2004GL021286

Tréhu, A.M., Long, P.E., Torres, M.E., Bohrmann, G., Rack, F.R., Collett, T.S., Goldberg, D.S., Milkov, A.V., Riedel, M., Schultheiss, P., Bangs, N.L., Barr, S.R., Borowski, W.S., Claypool, G.E., Delwiche, M.E., Dickens, G.R., Gracia, E., Guerin, G., Holland, M., Johnson, J.E., Lee, Y.-J., Liu, C.-S., Su, X., Teichert, B., Tomaru, H., Vanneste, M., Watanabe, M., Weinberger, J.L., 2004b. Three-dimensional distribution of gas hydrate beneath southern Hydrate Ridge: constraints from ODP Leg 204. Earth Planet. Sci. Lett. 222, 845–862. https://doi.org/10.1016/j.epsl.2004.03.035

Tryon, M.D., Brown, K.M., Torres, M.E., 2002. Fluid and chemical flux in and out of sediments hosting methane hydrate deposits on Hydrate Ridge, OR, II: Hydrological processes. Earth Planet. Sci. Lett. 201, 541–557. https://doi.org/10.1016/S0012-821X(02)00732-X

Tryon, M.D., Brown, K.M., Torres, M.E., Tréhu, A.M., McManus, J., Collier, R.W., 1999. Measurements of transience and downward fluid flow near episodic methane gas vents, Hydrate Ridge, Cascadia. Geology 27, 1075–1078. https://doi.org/10.1130/0091-7613(1999)027<1075:MOTADF>2.3.CO;2

Tsang-Hin-Sun, E., Batsi, E., Klingelhoefer, F., Géli, L., 2019. Spatial and temporal dynamics of gas-related processes in the Sea of Marmara monitored with ocean bottom seismometers. Geophys. J. Int. 216, 1989–2003. https://doi.org/10.1093/gji/ggy535

Wallmann, K., Riedel, M., Hong, W.L., Patton, H., Hubbard, A., Pape, T., Hsu, C.W., Schmidt, C., Johnson, J.E., Torres, M.E., Andreassen, K., Berndt, C., Bohrmann, G., 2018. Gas hydrate dissociation off Svalbard induced by isostatic rebound rather than global warming. Nat. Commun. 9, 1–9. https://doi.org/10.1038/s41467-017-02550-9

Wang, K., Davis, E.E., 1996. Theory for the propagation of tidally induced pore pressure variations in layered subseafloor formations. J. Geophys. Res. Solid Earth 101, 11483–11495. https://doi.org/10.1029/96JB00641

Wang, K., Davis, E.E., Kamp, G. van der, 1998. Theory for the effects of free gas in subsea formations on tidal pore pressure variations and seafloor displacements. J. Geophys. Res. Solid Earth 103, 12339–12353. https://doi.org/10.1029/98JB00952

Weber, T., Wiseman, N.A., Kock, A., 2019. Global ocean methane emissions dominated by shallow coastal waters. Nat. Commun. 10, 4584. https://doi.org/10.1038/s41467-019-12541-7

Wheeler, S.J., 1990. Movement of large gas bubbles in unsaturated fine-grained sediments. Mar. Geotechnol. 9, 113–129. https://doi.org/10.1080/10641199009388234

Xu, W., Germanovich, L.N., 2006. Excess pore pressure resulting from methane hydrate dissociation in marine sediments: A theoretical approach. J. Geophys. Res. 111, B01104. https://doi.org/10.1029/2004JB003600

Yamada, T., Prügel-Bennett, A., Thornton, B., 2021. Learning features from georeferenced seafloor imagery with location guided autoencoders. J. Field Robot. 38, 52–67. https://doi.org/10.1002/rob.21961

List of Figure Captions

Figure 1. Top left: Location of Southern Hydrate Ridge. Top right: Map of the primary infrastructure of the OOI Regional Cabled Array observatory (bathymetry data from GEBCO). Bottom: Overview map of the SHR summit with the location of the OOI Regional Cabled Array fiber optic cables, junction boxes and monitoring instruments. Shaded areas show the location of the main known vents. Bathymetric data were collected on an RCA survey cruise in 2008 with the AUV Sentry.

Figure 2. Temporal variations of the SHROS backscatter magnitude and CTD bottom pressure between July 6 and July 22, 2018 (top plots) and between October 19 and November 8, 2018 (bottom plots). The backscatter magnitude non-linearly reflects the strength of the gas bubble emissions. The bottom pressure plot shows the local mixed tidal regime with diurnal and semidiurnal constituents, as well as the fortnightly neap/spring tidal cycles. Bubble release is commonly stronger during ebb tide, and possibly also during spring tidal phases. However, some ebullition events do not correlate with the tide and may be triggered by local accumulation of pressurized free gas in the subsurface; the prominent peak observed on July 18, 2018 corresponded to the reactivation of the Summit-A vent after a very short venting interruption of about 4 h; it did not affect the other vents at the SHR summit and happened during flood tide within a neap tidal phase, hinting at shallow, local changes in the sediments.

Figure 3. a) Location of flare base points recorded with the SHROS between 6 July and 8 November 2018; the base points are grouped into clusters marking the location of the different SHR vent sites. b) Location of the main and periphery vents (see Discussion) overlain on the photomosaic; the main vent sites are all located on areas covered with microbial mats. c) Close-up view of the SHROS location and the Summit-A vent, with the 3D photomosaic in the background; a depression on the seafloor from ODP drill site 1949 (ODP Leg 204) can be seen in the top-left corner as well as in the bathymetric data. d) Close-up view of the 3D photomosaic at the Smokey Tavern vent showing the distribution of the microbial mats and the domed, collapsed and hummocky areas.

Figure 4. Power spectral density plots of the bottom pressure and SHROS data. Both datasets are dominated by the semi-diurnal constituents of the tide. For readability, the frequency units are shown in cycles per day (cpd), and the diurnal (O1, K1) and semi-diurnal (M2, N2, S2) harmonic constituents of the local tide are reported at the top of each plot.

Figure 5. SHROS magnitude data from 6 July to 22 July 2018 for each plume cluster (only active clusters are shown). The vertical axis is logarithmic to facilitate visualization of low magnitude variations. Absolute magnitude values cannot be compared between the clusters due to a distance bias (see text) and are not shown.

Figure 6. Top: consecutive 360° scans of the single-beam scanning sonar showing the start of a high-ebullition event at the Einstein's Grotto vent area. The high-ebullition event starts at three distinct bubble plumes consecutively; scans last about 3.5 minutes and are recorded clockwise starting from the North direction (0° azimuth angle). The timestamps correspond to the start times of the scans and the scan radii represent 10 m. Bottom: timeseries showing the variations over 24 h (14-15 November 2019) of the total magnitude of each full scan (continuous line) and the bottom pressure (dashed line). The four high ebullition events (peaks) occurred either during ebb tide or at the ebb tide turning point. Each high ebullition event is marked by a sudden onset and a slow decay; the largest peak corresponds to the ebullition event illustrated in the top six scan images.

Figure 7. Variations of the SHROS magnitude of the Einstein's Grotto vent (dashed black line) and the CAMDSB103 image-based bubble counts (red line). The timing of acoustic data peaks coincide well with bubble count peaks. Some bubble count peaks were not detected by the sonar because it has a lower sampling frequency (Ts = 2 h) than the camera (Ts = 30 min). The height of the peaks cannot be compared because the sonar monitors all plumes occurring within the entire Einstein's Grotto vent area, whereas the camera focuses on the base of a single plume. Bubble counts lower than about 5 are below the accuracy of the counting method and might be caused by false detection of bubble objects.

Figure 8. A pressure outburst was documented by the CAMDSB103 camera on July 23, 2018. The camera images show sediment resuspension shortly (0 to 30 minutes) after the outburst. Images taken after visibility improved show significant seabed changes including the presence of a large well-lithified sediment block into the collapsed area subsequent to the blow out. Scanning-sonar scans recorded before and after the event show that the seabed morphology at the location of the outburst changed over an area of at least 3 m². The hummocky area east of the sonar is part of the Einstein's Grotto vent. The range of the sonar scans is 20 m. The laser pointers on the camera images are 10 cm apart. In the difference plot, blue and red colors show negative and positive differences respectively.

Figure 9. Left: progressive vector diagram showing the direction of water particle movement from Oct 5 at 18:00 (plot origin) until Oct 9 at 18:00. The red segments highlight times when upwelling flow were recorded by the ADCP. Right: ADCP current velocities and bottom pressure data for the same time period as in the progressive vector diagram. The white areas, marking data gaps in the velocity plots are mainly caused by the presence of bubble plumes across the acoustic beams of the ADCP (Philip et al., 2016b). The grey bands in the pressure plot indicate the timing of the bubble-induced upwelling flows imaged by the ADCP. The progressive vector diagram clearly shows that upwelling flows are only recorded by the ADCP when the dominant northward component of the bottom currents is weak or reversed. Considering that the ADCP is located to the south-southwest of the main vents, the tidally-influenced northward currents deflect bubble plumes away from the ADCP, explaining why upwelling flows are rarely detected during flood tides.

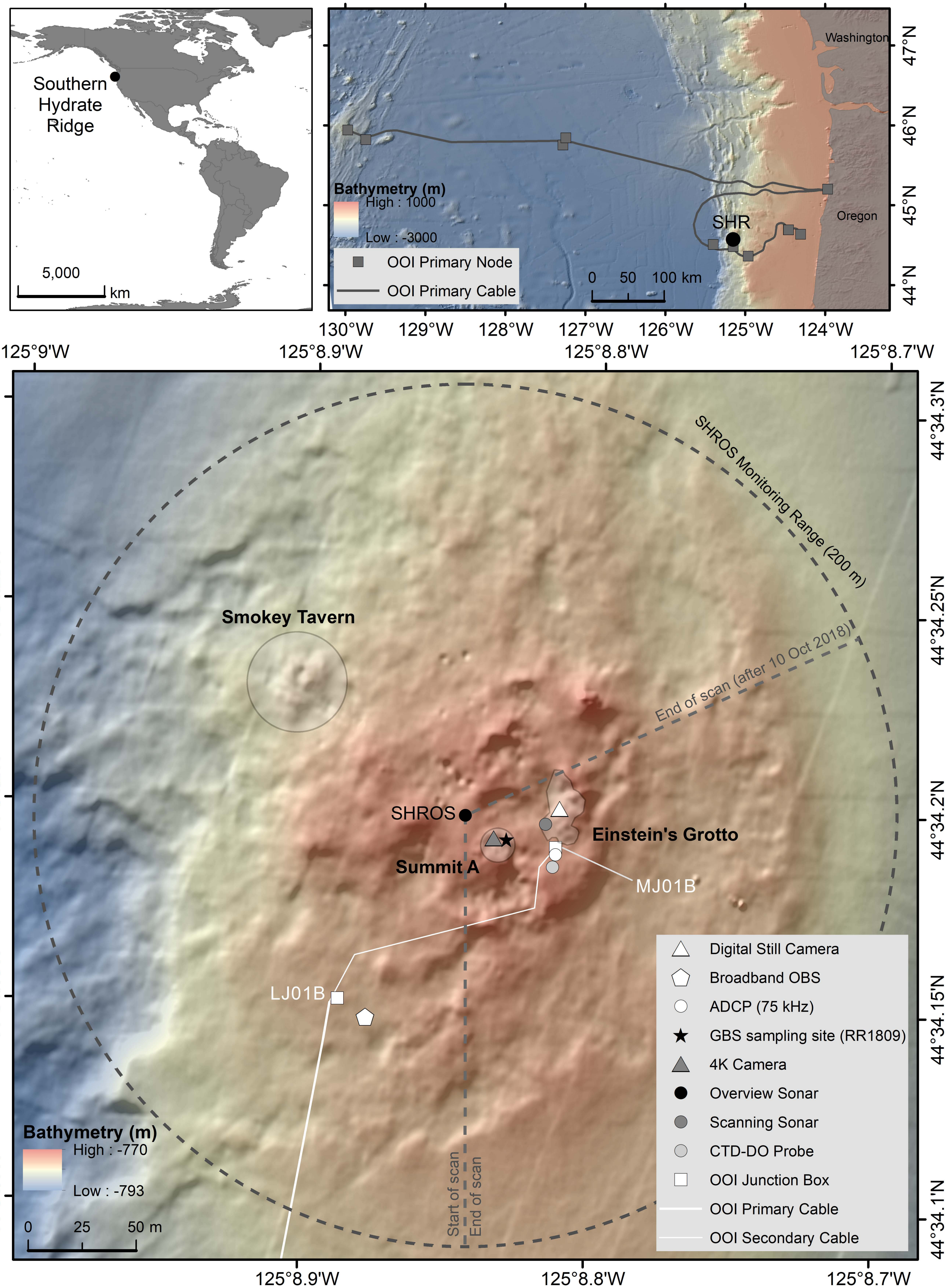

Southern Hydrate Ridge
5,000 km
Washington
Oregon
47°N
46°N
45°N
44°N
130°W
129°W
128°W
127°W
126°W
125°W
124°W
Bathymetry (m)
High : 1000
Low : -3000
OOI Primary Node
OOI Primary Cable
SHR
0 50 100 km
125°9'W
125°8.9'W
125°8.8'W
125°8.7'W
44°34.3'N
44°34.25'N
44°34.2'N
44°34.15'N
44°34.1'N
SHROS Monitoring Range (200 m)
Smokey Tavern
End of scan (after 10 Oct 2018)
SHROS
Einstein's Grotto
Summit A
MJ01B
LJ01B
Start of scan
End of scan
Bathymetry (m)
High : -770
Low : -793
0 25 50 m
Digital Still Camera
Broadband OBS
ADCP (75 kHz)
GBS sampling site (RR1809)
4K Camera
Overview Sonar
Scanning Sonar
CTD-DO Probe
OOI Junction Box
OOI Primary Cable
OOI Secondary Cable

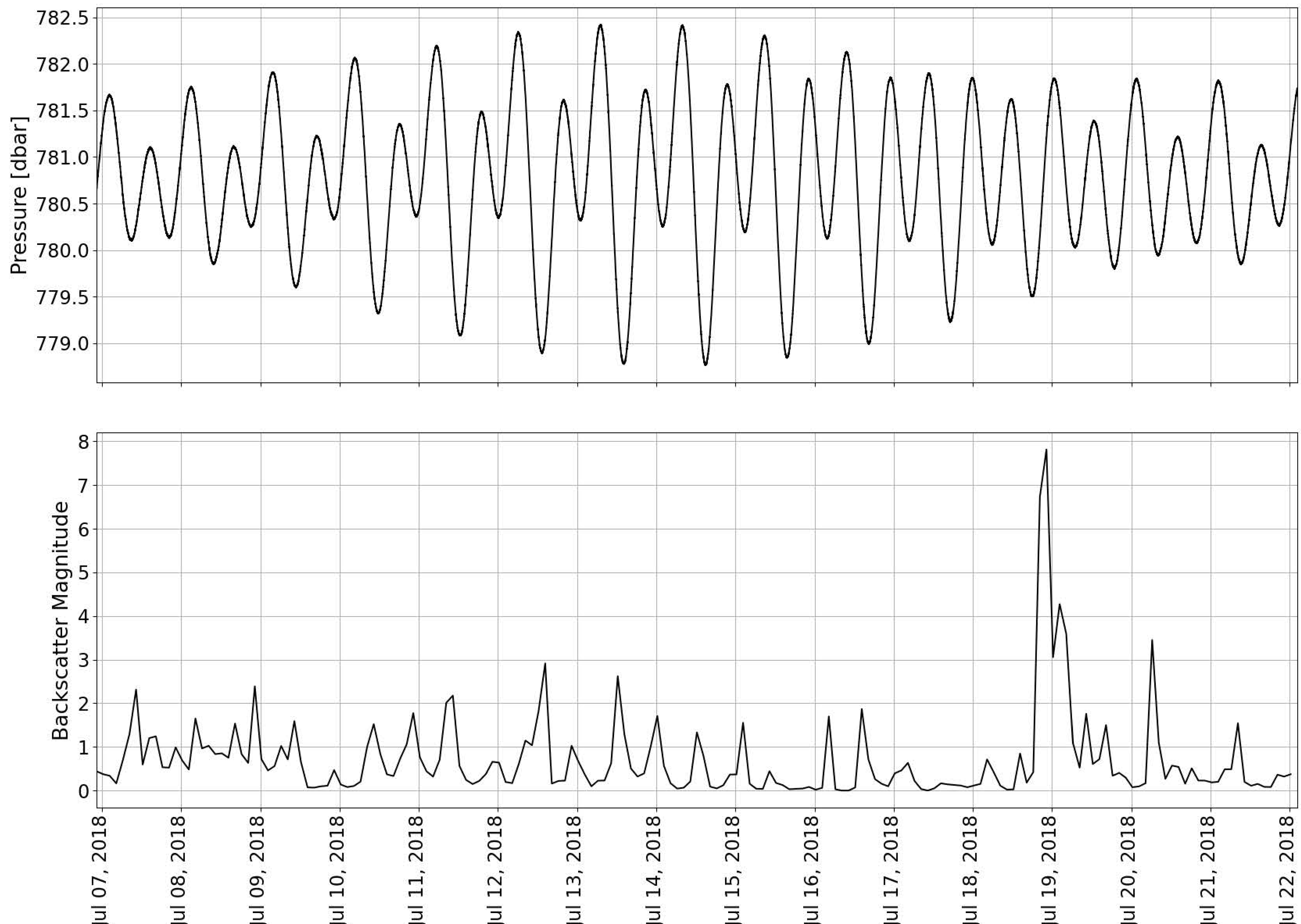
Pressure [dbar]
782.5
782.0
781.5
781.0
780.5
780.0
779.5
779.0
Backscatter Magnitude
8
7
6
5
4
3
2
1
0
Jul 07, 2018
Jul 08, 2018
Jul 09, 2018
Jul 10, 2018
Jul 11, 2018
Jul 12, 2018
Jul 13, 2018
Jul 14, 2018
Jul 15, 2018
Jul 16, 2018
Jul 17, 2018
Jul 18, 2018
Jul 19, 2018
Jul 20, 2018
Jul 21, 2018
Jul 22, 2018

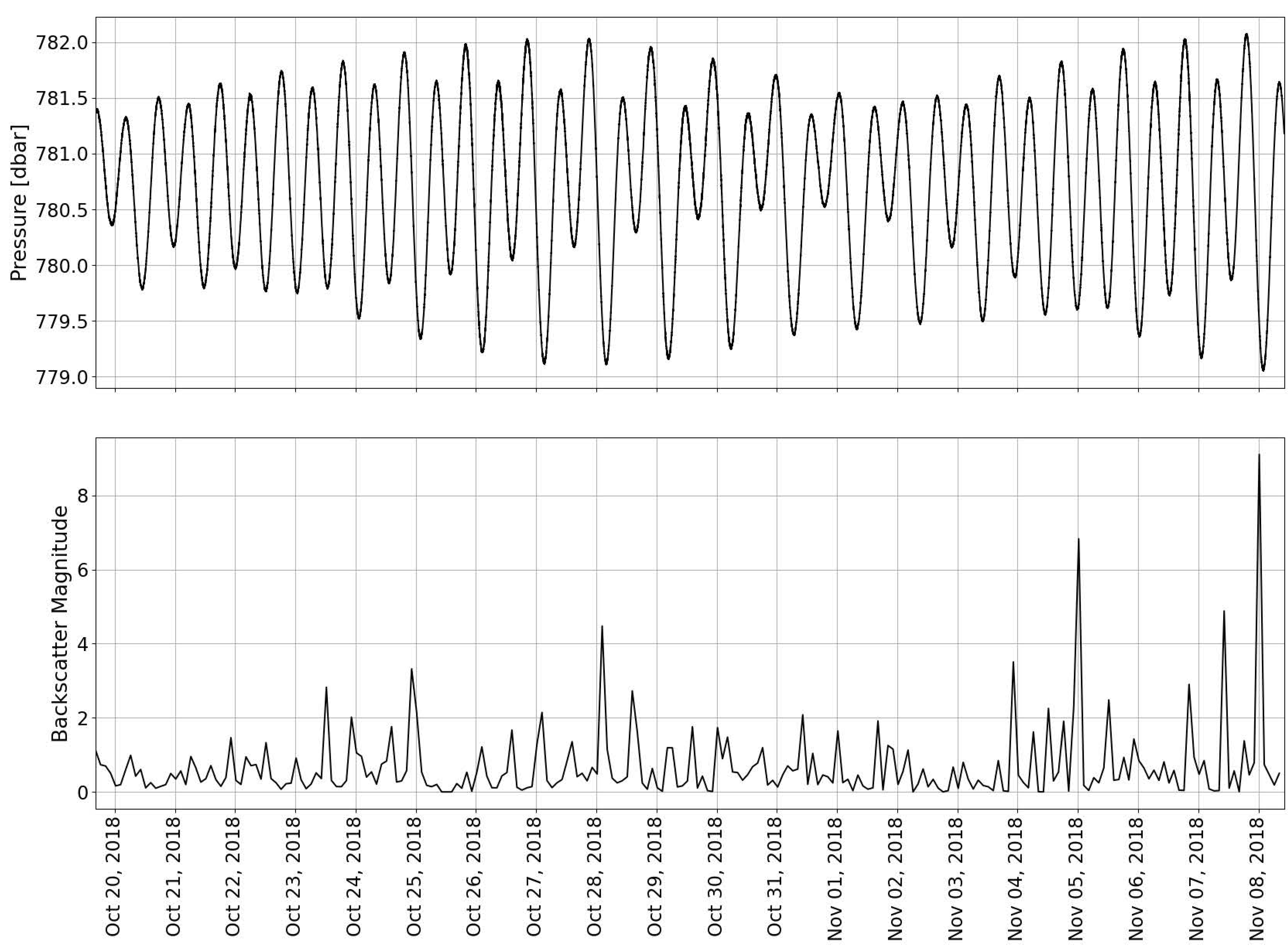
Pressure [dbar]
782.0
781.5
781.0
780.5
780.0
779.5
779.0
Backscatter Magnitude
8
6
4
2
0
Oct 20, 2018
Oct 21, 2018
Oct 22, 2018
Oct 23, 2018
Oct 24, 2018
Oct 25, 2018
Oct 26, 2018
Oct 27, 2018
Oct 28, 2018
Oct 29, 2018
Oct 30, 2018
Oct 31, 2018
Nov 01, 2018
Nov 02, 2018
Nov 03, 2018
Nov 04, 2018
Nov 05, 2018
Nov 06, 2018
Nov 07, 2018
Nov 08, 2018

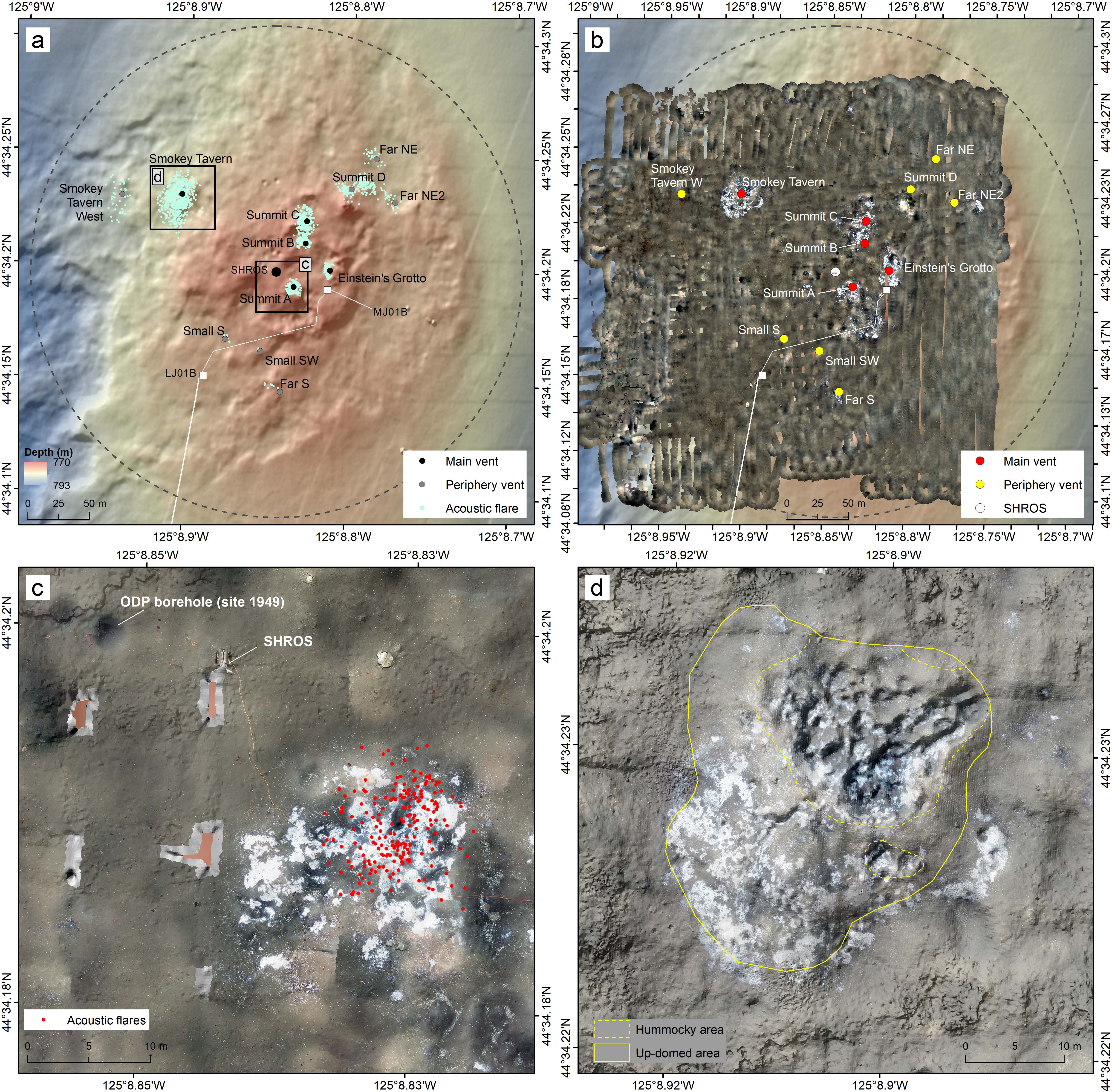

a
Smokey Tavern
Smokey Tavern West
d
Far NE
Summit D
Far NE2
Summit C
Summit B
SHROS
c
Einstein's Grotto
Summit A
MJ01B
Small S
Small SW
LJ01B
Far S
Depth (m)
770
793
0 25 50 m
Main vent
Periphery vent
Acoustic flare
b
Smokey Tavern W
Smokey Tavern
Far NE
Summit D
Far NE2
Summit C
Summit B
Einstein's Grotto
Summit A
Small S
Small SW
Far S
Main vent
Periphery vent
SHROS
c
ODP borehole (site 1949)
SHROS
Acoustic flares
0 5 10 m
d
Hummocky area
Up-domed area
0 5 10 m

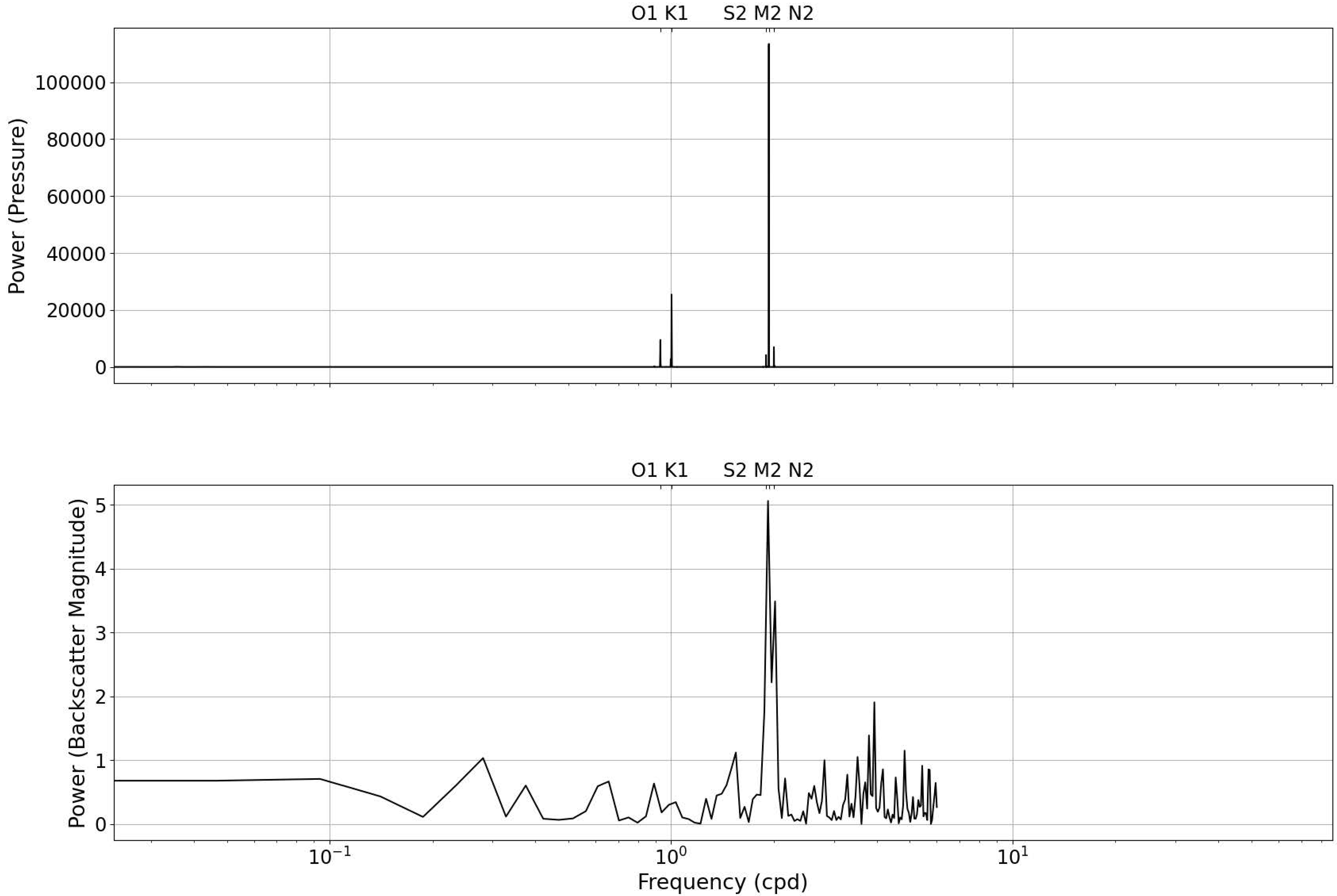
O1 K1 S2 M2 N2
Power (Pressure)
100000
80000
60000
40000
20000
0
O1 K1 S2 M2 N2
Power (Backscatter Magnitude)
5
4
3
2
1
0
10^{-1}
10^{0}
10^{1}
Frequency (cpd)

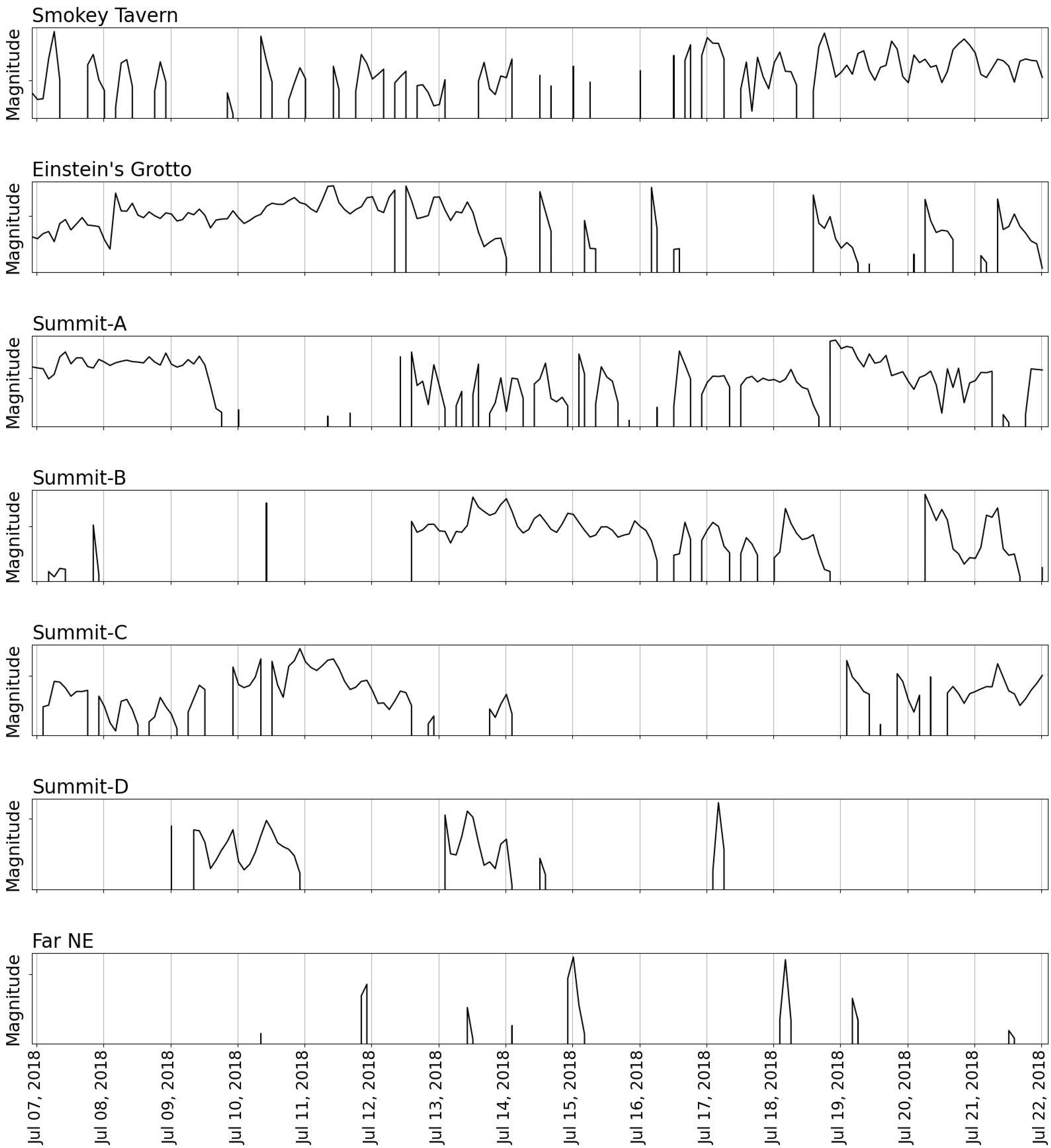
Smokey Tavern
Einstein's Grotto
Summit-A
Summit-B
Summit-C
Summit-D
Far NE
Magnitude
Jul 07, 2018
Jul 08, 2018
Jul 09, 2018
Jul 10, 2018
Jul 11, 2018
Jul 12, 2018
Jul 13, 2018
Jul 14, 2018
Jul 15, 2018
Jul 16, 2018
Jul 17, 2018
Jul 18, 2018
Jul 19, 2018
Jul 20, 2018
Jul 21, 2018
Jul 22, 2018

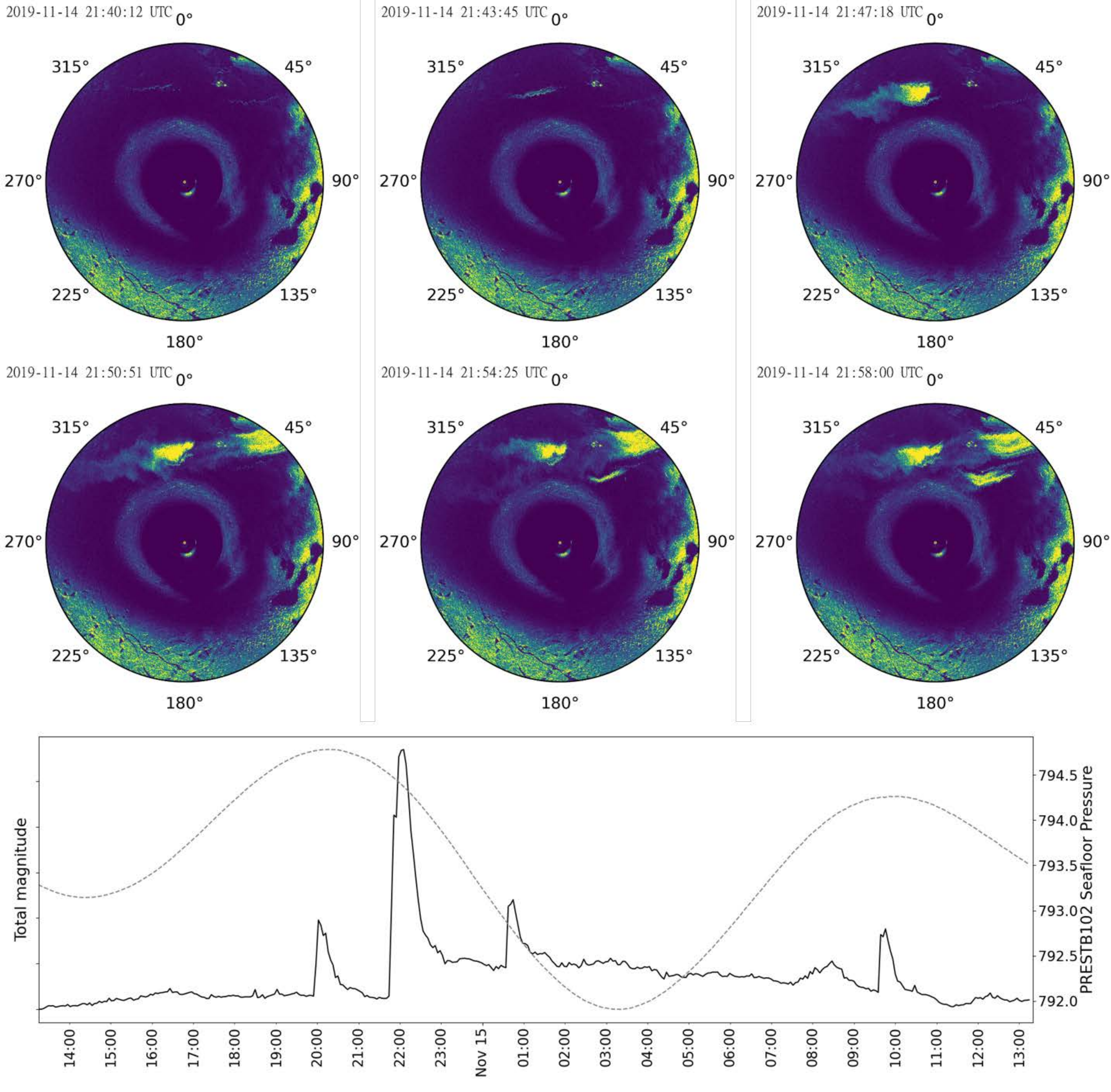

2019-11-14 21:40:12 UTC
2019-11-14 21:43:45 UTC
2019-11-14 21:47:18 UTC
2019-11-14 21:50:51 UTC
2019-11-14 21:54:25 UTC
2019-11-14 21:58:00 UTC
0°
45°
90°
135°
180°
225°
270°
315°
Total magnitude
PRESTB102 Seafloor Pressure
794.5
794.0
793.5
793.0
792.5
792.0
14:00
15:00
16:00
17:00
18:00
19:00
20:00
21:00
22:00
23:00
Nov 15
01:00
02:00
03:00
04:00
05:00
06:00
07:00
08:00
09:00
10:00
11:00
12:00
13:00

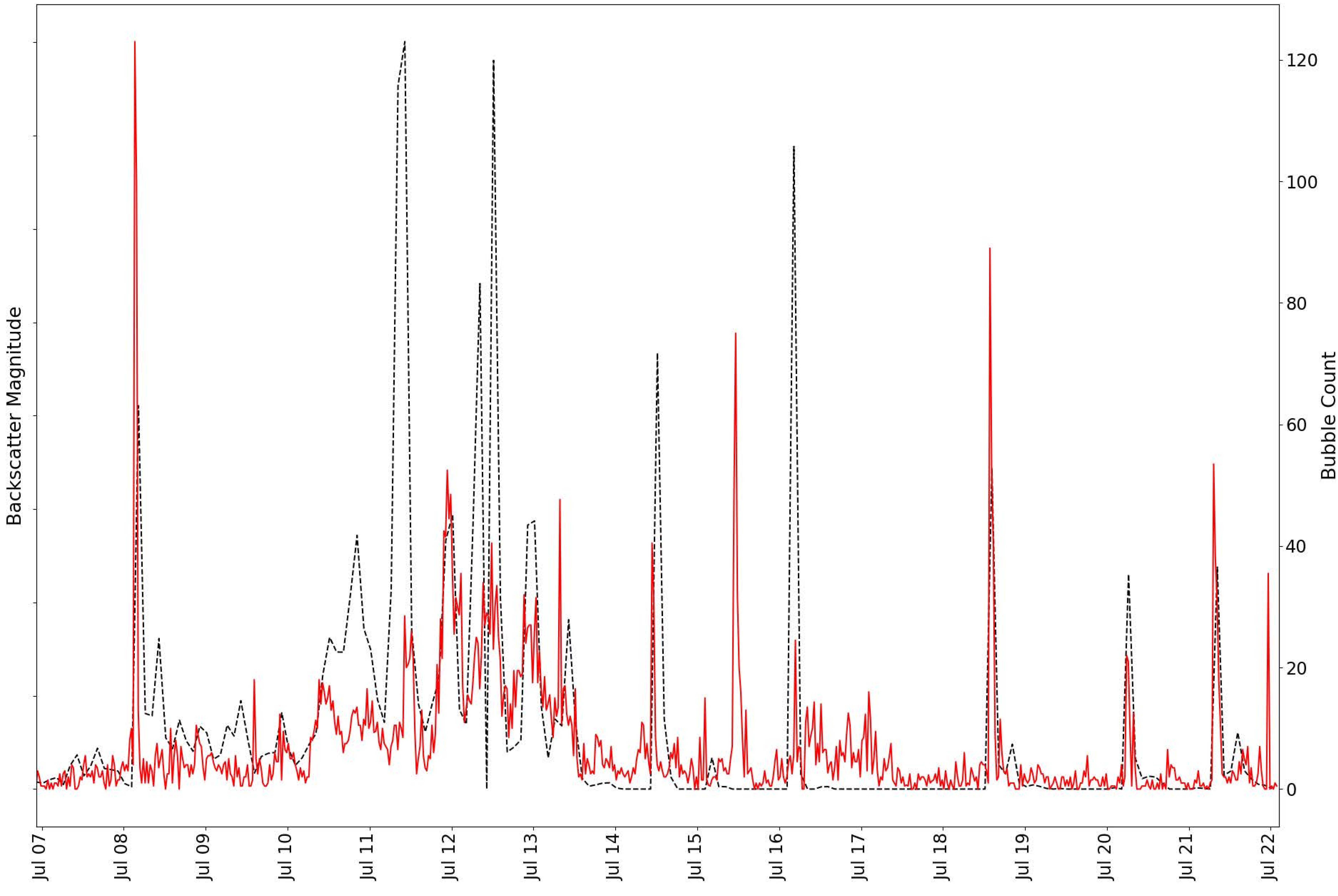

Backscatter Magnitude
Bubble Count
0
20
40
60
80
100
120
Jul 07
Jul 08
Jul 09
Jul 10
Jul 11
Jul 12
Jul 13
Jul 14
Jul 15
Jul 16
Jul 17
Jul 18
Jul 19
Jul 20
Jul 21
Jul 22

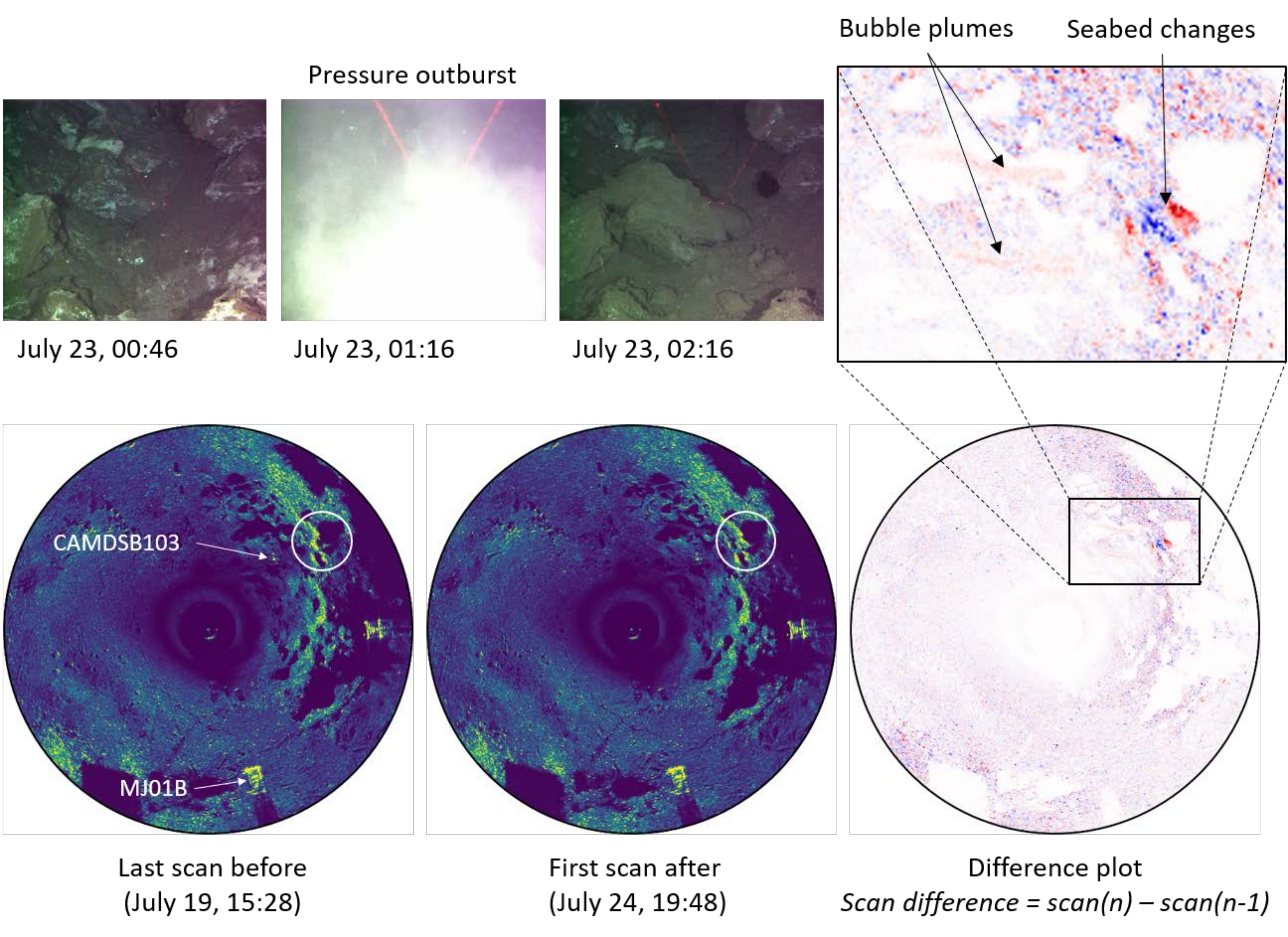
Pressure outburst
July 23, 00:46
July 23, 01:16
July 23, 02:16
Bubble plumes
Seabed changes
CAMDSB103
MJ01B
Last scan before
(July 19, 15:28)
First scan after
(July 24, 19:48)
Difference plot
Scan difference = scan(n) – scan(n-1)

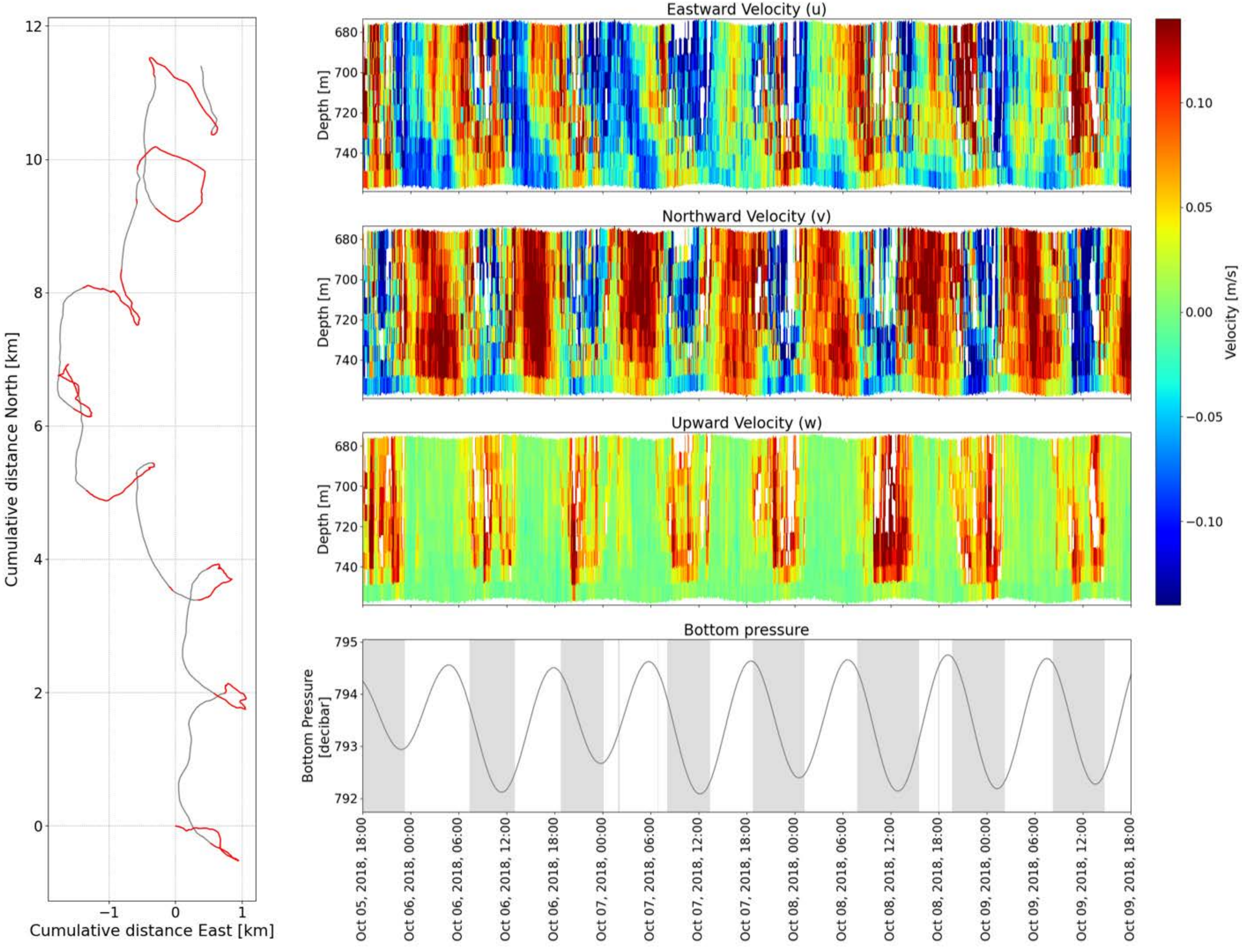

Eastward Velocity (u)
Northward Velocity (v)
Upward Velocity (w)
Bottom pressure
Depth [m]
Velocity [m/s]
Bottom Pressure [decibar]
Cumulative distance North [km]
Cumulative distance East [km]
Oct 05, 2018, 18:00
Oct 06, 2018, 00:00
Oct 06, 2018, 06:00
Oct 06, 2018, 12:00
Oct 06, 2018, 18:00
Oct 07, 2018, 00:00
Oct 07, 2018, 06:00
Oct 07, 2018, 12:00
Oct 07, 2018, 18:00
Oct 08, 2018, 00:00
Oct 08, 2018, 06:00
Oct 08, 2018, 12:00
Oct 08, 2018, 18:00
Oct 09, 2018, 00:00
Oct 09, 2018, 06:00
Oct 09, 2018, 12:00
Oct 09, 2018, 18:00